L-87-67-2

STEADY AND UNSTEADY TERMINAL-SHOCK AERODYNAMICS ON CONE-CYLINDER BODIES

October 1967

Prepared by: Lars Eric Ericsson
Lars E. Ericsson
Flight Technology

Approved by: M. Tucker
M. Tucker, Manager
Flight Technology

Prepared Under Contract NAS 8-20354
for
Aerodynamics Division
Aero-Astrodynamics Laboratory
George C. Marshall Space Flight Center
Huntsville, Alabama

LOCKHEED MISSILES & SPACE COMPANY

ABSTRACT

The effects of shock-induced boundary-layer separation on cone-cylinder body aerodynamics have been studied. At high subsonic speeds, the local supersonic flow region aft of the cone-cylinder shoulder is terminated by a normal shock. The resulting boundary-layer separation is shown to change the vehicle aerodynamics appreciably. At a certain critical angle-of-attack, complete leeward-side flow separation occurs which drastically affects the vehicle dynamics, in particular elastic vehicle dynamics. Analytical methods are developed that relate steady and unsteady aerodynamics for the two types of flow separation.

SUMMARY

At high subsonic speeds, even slender cone-cylinder bodies experience flow separation. The flow expands to supersonic speeds when passing the cone-cylinder shoulder. The supersonic region is terminated by a normal shock that causes the boundary layer to separate. At increasing angle-of-attack, the leeward boundary layer is thickened and more easily separated, resulting in a forward movement of the shock. On the windward side, opposite effects occur, and a negative forebody load is generated that moderately affects the vehicle dynamics. When the angle-of-attack exceeds a critical value, the leeward-side boundary layer can nowhere support the shock, and complete flow separation occurs aft of the cone-cylinder shoulder. The associated jumpwise load change is shown to severely affect vehicle dynamics.

CONTENTS

ILLUSTRATIONS

Section 1

INTRODUCTION

Slender cone-cylinder bodies are usually not expected to cause the aerodynamicist any problems. The only problem arises in a very narrow speed range at high subsonic speeds. At these speeds, the normal shock terminating the local supersonic speed region aft of the cone-cylinder shoulder causes boundary-layer separation. When the angle-of-attack (or nose-cone half angle) is increased, the separation suddenly jumps forward to the cone-cylinder shoulder. The associated change of the aerodynamic loads is large, especially in the unsteady case.

Section 2
STATEMENT OF PROBLEM

Experimental data obtained by Robertson and Chevalier (Ref. 1) reveal the following distinct terminal shock characteristics on cone-cylinder bodies: At high subsonic speeds, a terminal shock appears downstream of the cone-cylinder shoulder causing local boundary-layer separation (Fig. 2-1). When the angle-of-attack is increased to 4°, the leeward-side separation jumps forward to the cone-cylinder shoulder. The large jumpwise load change can best be appreciated by comparing it with the pressure change when the angle-of-attack is increased from zero to $\alpha = 2°$. The jump to complete leeward-side separation occurs at higher angles-of-attack the more slender the conical forebody is (Fig. 2-2).

Figure 2-3 shows another characteristic of the interaction between the terminal shock and the boundary layer. The leeward-side shock moves forward of the windward-side shock, thereby creating a negative cylinder load. The terminal shock moves back with increasing Mach number and with increasing cone angle (Figs. 2-4 and 2-5). Figure 2-6, in form of a carpet plot (Refs. 2 and 3), illustrates the opposite effects of increasing Mach number and increasing angle-of-attack.

The resultant problem may be described as follows: In inviscid flow, the effects of increasing Mach number and increasing angle-of-attack on the leeward-side shock movement would be the same, both causing the shock to move downstream. The forward movement of the leeward-side shock in viscous flow results because the leeward-side boundary layer is thickened and weakened (thinner profile) when forebody cross-flow occurs. Since the unsteady aerodynamic characteristics for inviscid (attached flow) and for viscous (separated) flow are drastically different (Refs. 4 and 5), ability to discriminate between viscous and inviscid effects is essential. The purpose of this report is to illustrate how this discrimination can be accomplished for cone-cylinder bodies.

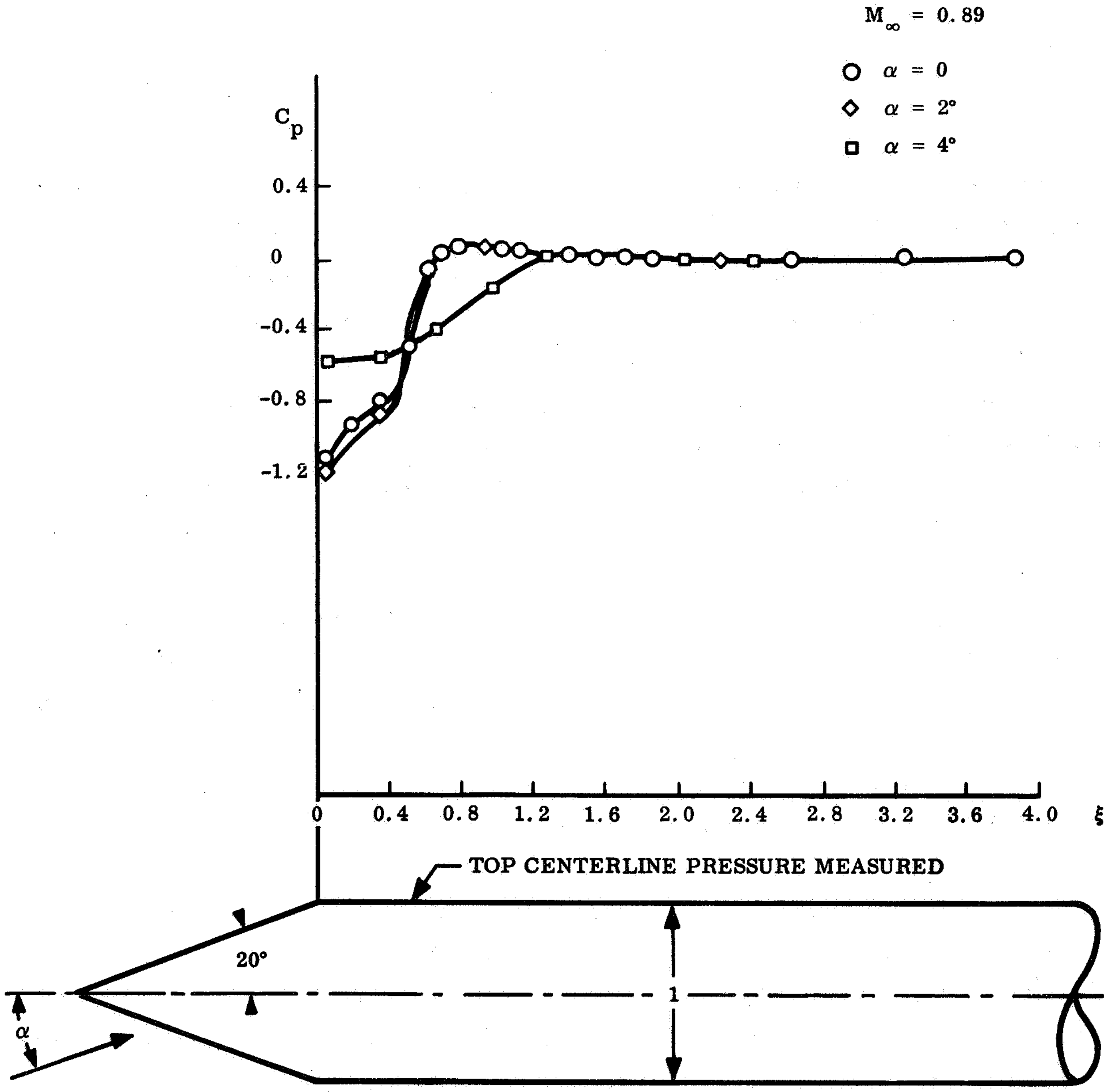

Fig. 2-1 Aerodynamic Characteristics at M_∞ = 0.89 of a 20° Cone-Cylinder Body With Separated Flow

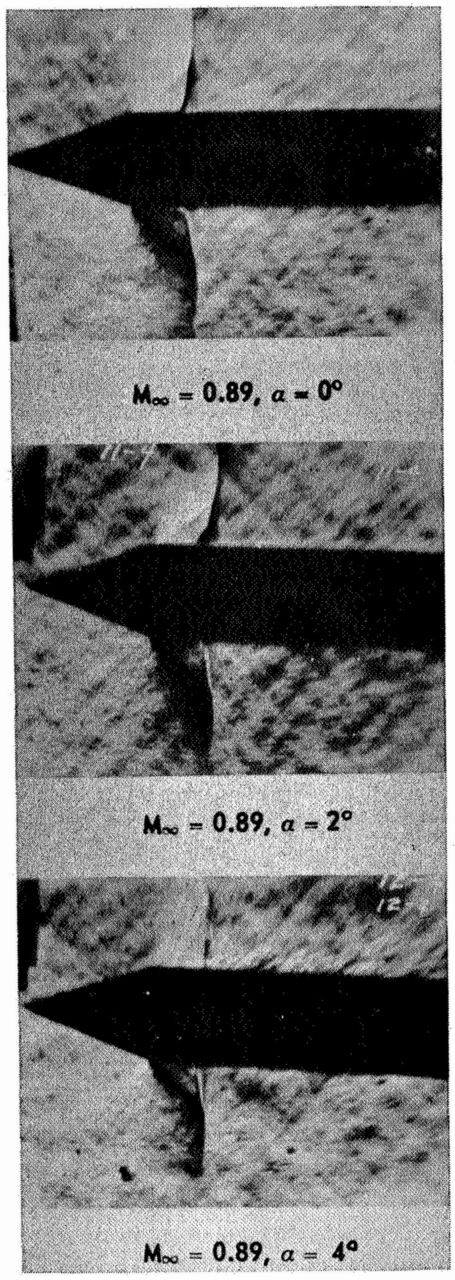

Fig. 2-1 Aerodynamic Characteristics at $M_\infty = 0.89$ of a 20° Cone-Cylinder Body With Separated Flow (Cont.)

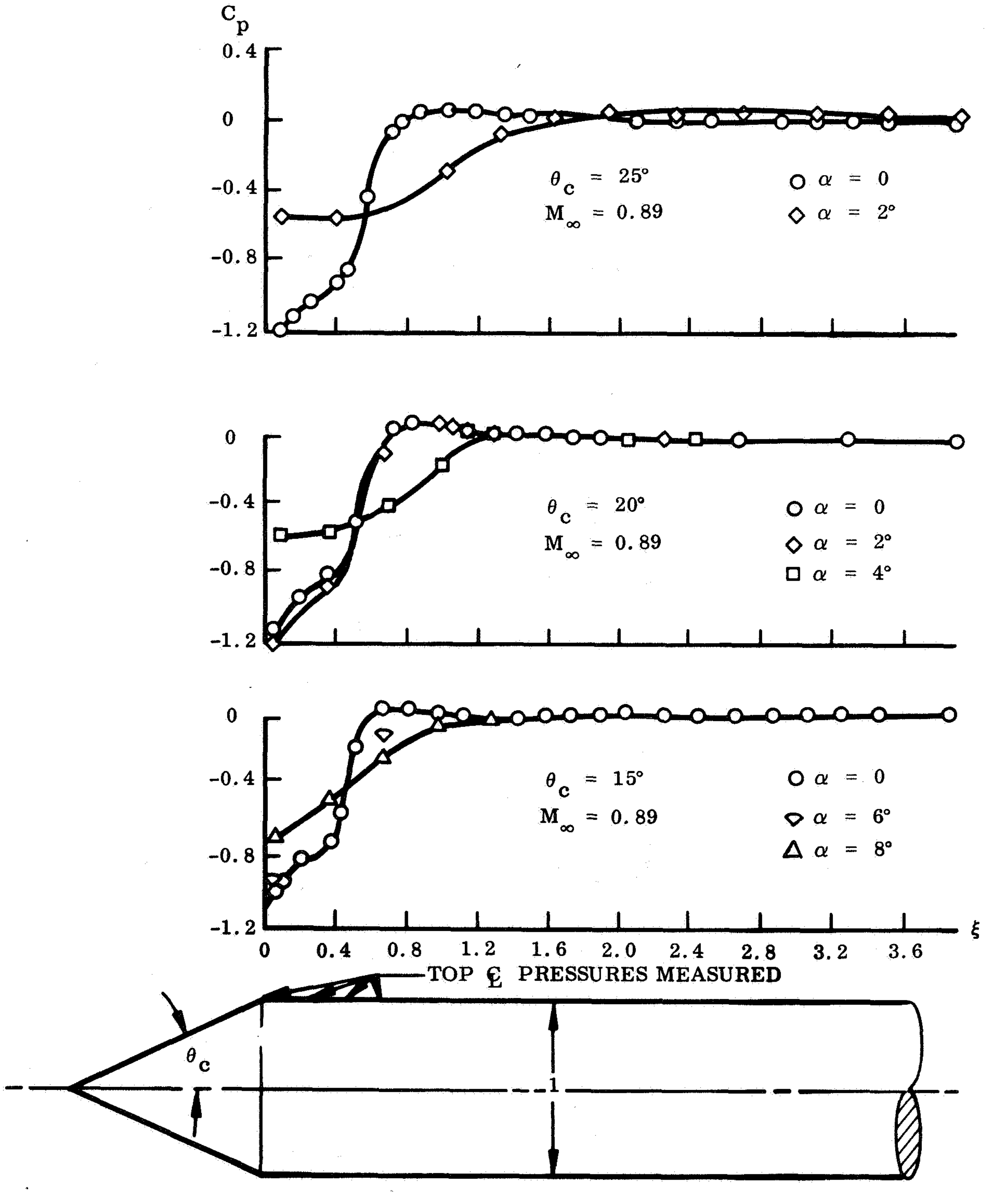

Fig. 2-2 Effect of Cone Angle on Occurrence of Complete Flow Separation at M_∞ = 0.89

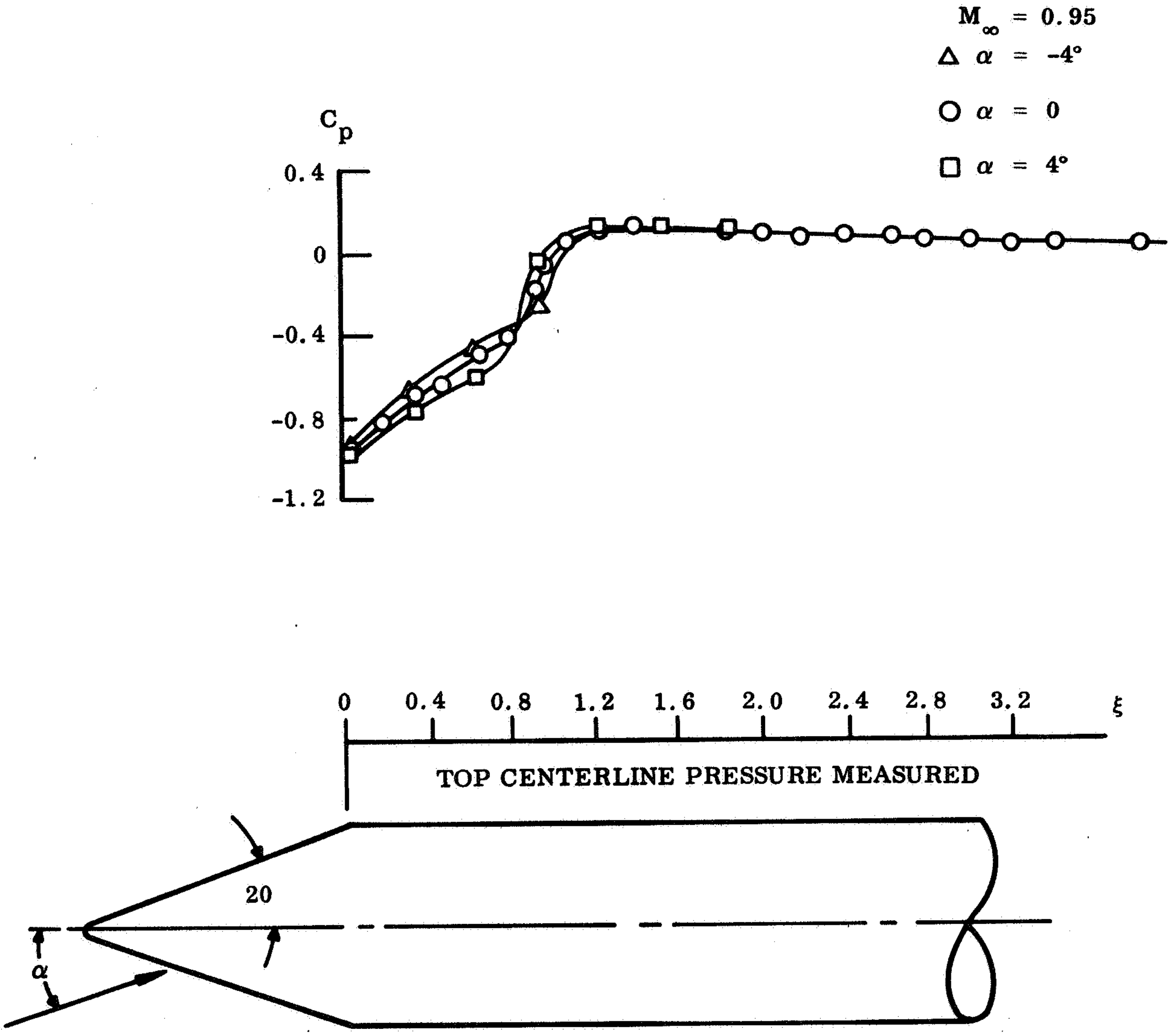

Fig. 2-3 Effect of Angle-of-Attack on Terminal-Shock Location on a 20° Cone-Cylinder Body at M_∞ = 0.95

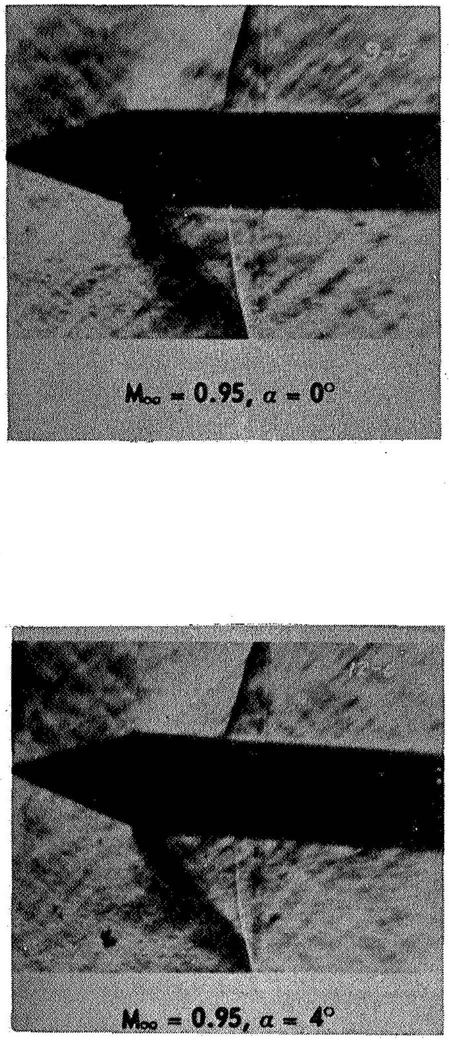

Fig. 2-3 Effect of Angle-of-Attack on Terminal-Shock Location on a 20° Cone-Cylinder Body at $M_\infty = 0.95$ (Cont.)

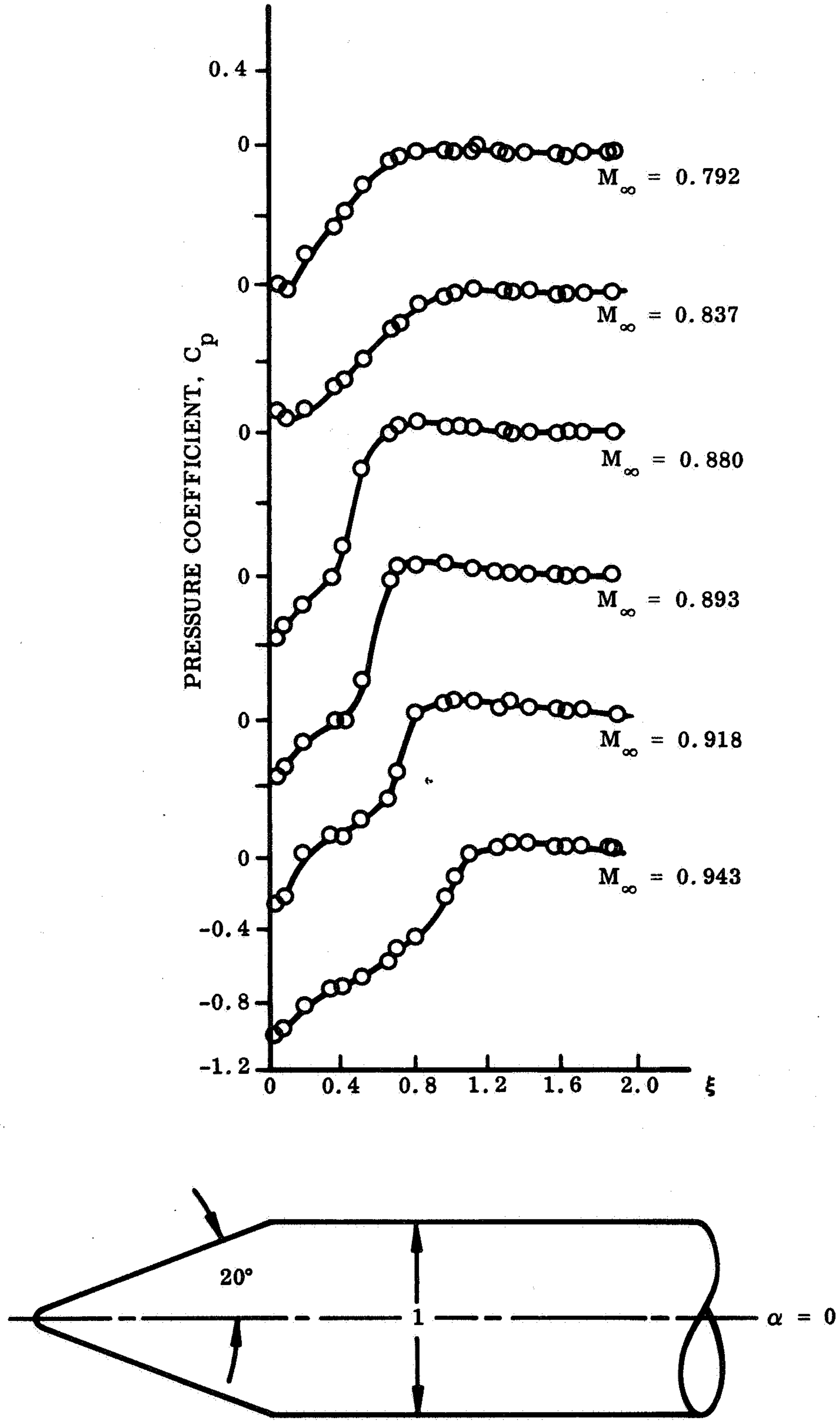

Fig. 2-4 Effect of Mach Number on Terminal-Shock Location on a 20° Cone-Cylinder Body at α = 0

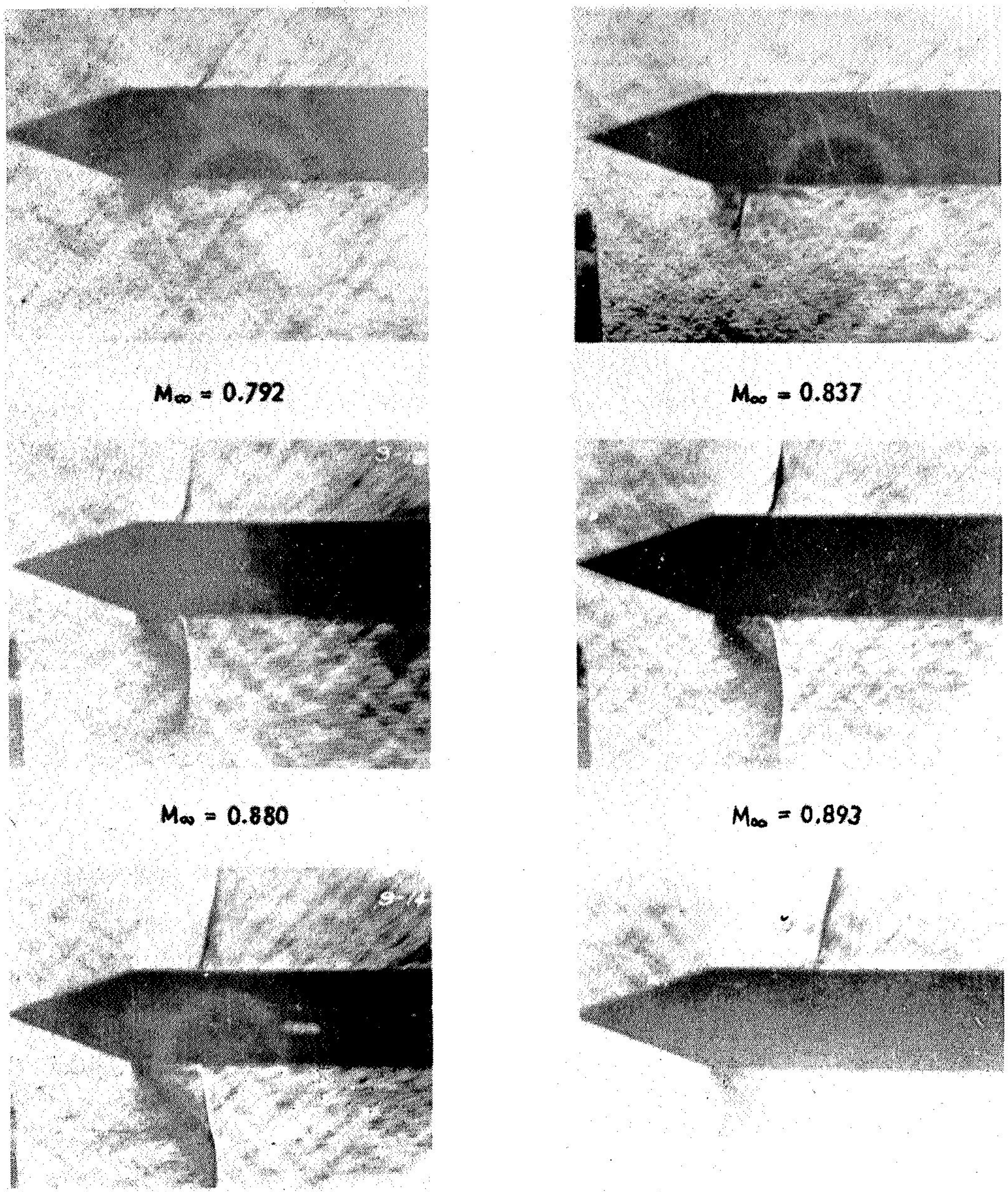

$M_\infty = 0.792$ $M_\infty = 0.837$

$M_\infty = 0.880$ $M_\infty = 0.893$

$M_\infty = 0.918$ $M_\infty = 0.943$

Fig. 2-4 Effect of Mach Number on Terminal-Shock Location on a 20° Cone-Cylinder Body at $\alpha = 0$ (Cont.)

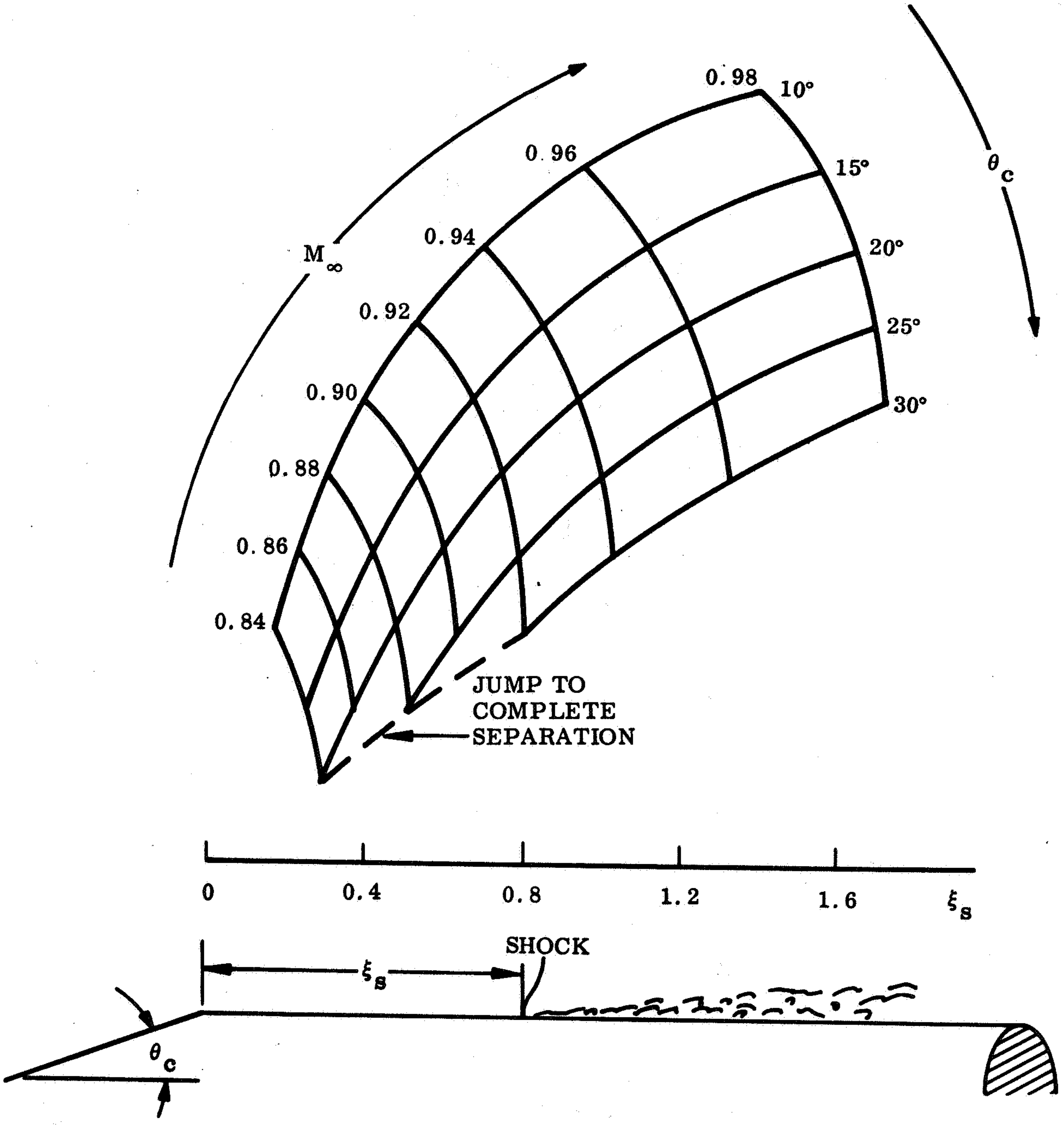

Fig. 2-5 Combined Effect of Mach Number and Cone Angle on the Terminal-Shock Location on Cone-Cylinder Bodies at $\alpha = 0$

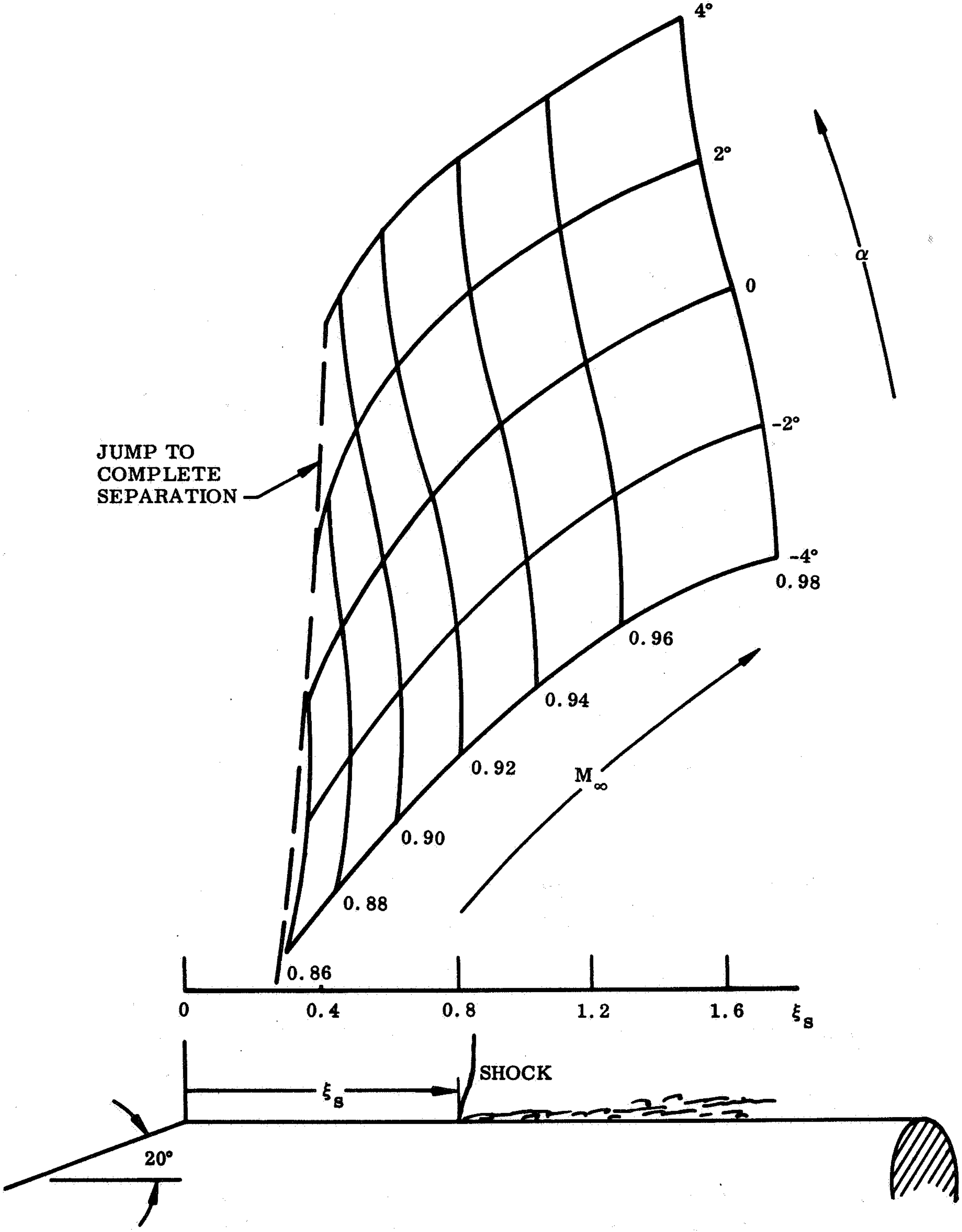

Fig. 2-6 Combined Effect of Mach Number and Angle-of-Attack on the Terminal-Shock Location on a 20° Cone-Cylinder Body

Section 3
ANALYTIC APPROACH

3.1 INTRODUCTION

The shock-boundary layer interaction, i.e., the viscous effects on the terminal shock aerodynamics, will be governed mainly by how the approaching boundary layer is affected by forebody crossflow and by external axial velocity gradient. That is, in a first approximation, the terminal shock strength can be assumed constant for small angle-of-attack changes. On the leeward side, an increasing angle-of-attack will produce an increasingly thick boundary layer as well as an increasingly adverse pressure gradient. The consequently weakened boundary layer profile cannot negotiate the pressure jump through the shock. The shock therefore moves forward to a location where the boundary layer is strong enough to accept it (Figs. 2-3 and 2-6). In proximity of the cone-cylinder shoulder with the sharply increasing adverse pressure gradient, no such equilibrium location can be found. Thus, the shock jumps all the way forward to the cone-cylinder shoulder, with a resultant sudden and complete flow separation on the leeward side (Fig. 2-1).

With the assumption of constant shock strength, analytic relations will be developed to relate the unsteady aerodynamics of shock-boundary layer interaction to its static aerodynamic characteristics. The following pages will also describe how the needed discrimination is accomplished between viscous and inviscid static characteristics.

3.2 STEADY TERMINAL-SHOCK AERODYNAMICS

The pressure distributions in Fig. 2-4 show some slight overpressure behind the shock followed by an expansion down to free-stream pressure. The overpressure is due to the separated flow wedge, and, in inviscid flow the pressure aft of the shock would be the free-stream pressure as sketched in Fig. 3-1. (As will be shown later, the over-pressure due to boundary layer thickening in attached flow is negligible.) The pressure distributions in Fig. 2-4 indicate that the terminal shock is strong and can be treated as a normal shock. Thus, the pressure jump $p_1/\hat{p}_1 = p_1/p_\infty$ through the shock can be computed using normal shock relations (Ref. 6).

$$\left.\begin{aligned} p_1/H_\infty &= (p_\infty/H_\infty)(p_1/\hat{p}_1) \\ \left(p_1/\hat{p}_1\right)^{-1} &= [2\gamma/(\gamma + 1)] \left[M_1^2 - (\gamma - 1)/2\gamma\right] \\ M_1^2 &= \gamma^{-1} \left\{1 + [(\gamma - 1)/2]\, M_\infty^2\right\} \left[M_\infty^2 - (\gamma - 1)/2\gamma\right]^{-1} \end{aligned}\right\} \qquad (3.1)$$

That is,

$$P_1 = (p_1 - p_\infty)/H_\infty = -(p_\infty/H_\infty)/(1 - p_1/\hat{p}_1)$$

$$P_1 = -\left[M_\infty^2 - (\gamma - 1)/2\gamma\right]\left(1 - M_\infty^2\right)^{-1}\left\{1 + [(\gamma - 1)/2]\, M_\infty^2\right\}^{-\gamma/(\gamma-1)} \qquad (3.2)$$

If the inviscid pressure distribution $P(\xi)$ ahead of the shock were known, the terminal-shock location ξ_{sh} in inviscid flow would be determined by

$$P(\xi_{sh}) = P_1 \qquad (3.3)$$

Static data for cone-cylinder bodies at high subsonic and transonic speeds (Ref. 1) show the $P(\xi)$-distributions for various cone angles to be very similar (Fig. 3-2). Borrowing Syverton's and Dennis' concept of exponential decay from the shoulder pressure P_o (Ref. 7), one may express $P(\xi)$ as follows:

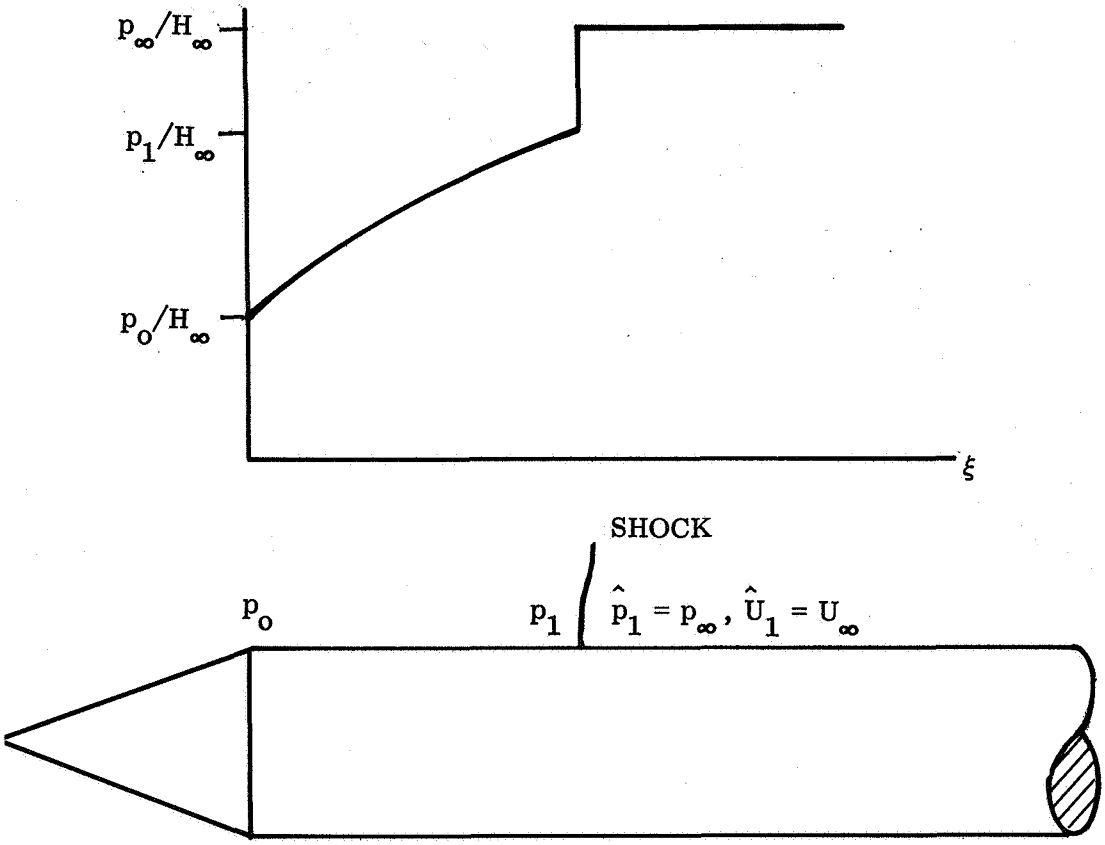

Fig. 3-1 Sketch of Inviscid Terminal-Shock Aerodynamics

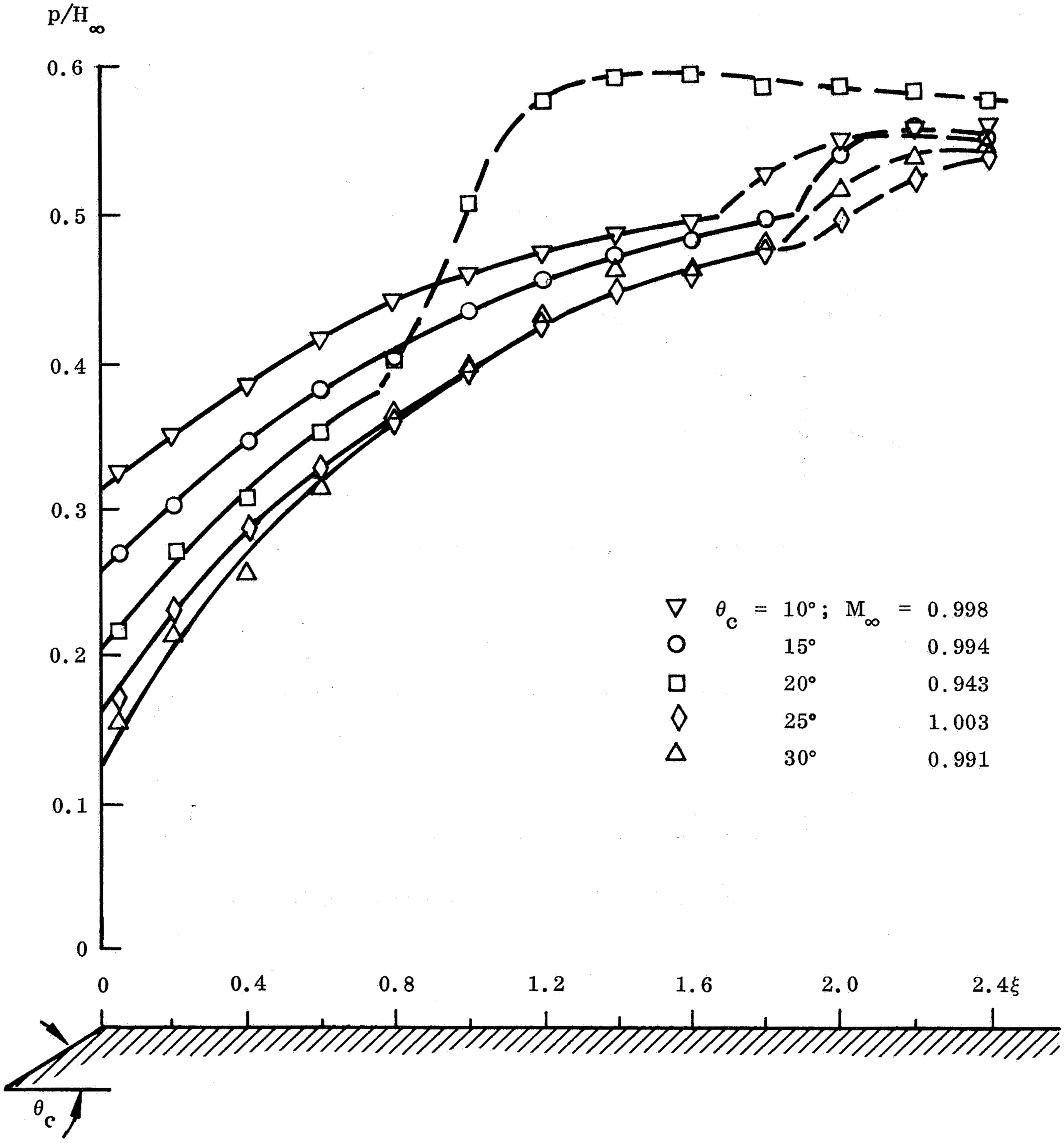

Fig. 3-2 Transonic Pressure Distributions Over Cone-Cylinder Bodies at $\alpha = 0$

$$P = P_o e^{-\left(\frac{\partial P}{\partial \xi}\right)_o \xi / P_o} \tag{3.4}$$

Defining $(\partial P/\partial \xi)_o$ as (see Fig. 3-3)

$$(\partial P/\partial \xi)_o = - P_o/\xi_o \tag{3.5}$$

makes $P(\xi)$ take the following simple form:

$$P(\xi) = P_o e^{-\xi/\xi_o} \tag{3.6}$$

That is, $P(\xi)$ is determined uniquely by the two parameters P_o and ξ_o. The pressure distributions in Fig. 3-2 (Ref. 1) are well correlated by one ξ_o-value (Fig. 3-4). Also data obtained at lower Mach numbers and by other investigators (Ref. 8) indicate that $P(\xi)$ is satisfactorily given by Eq. (3.6) using a value of $\xi_o = 0.9$ independent of θ_c and M_∞ (Fig. 3-4b).

Combining Eqs. (3.3) and (3.6) gives the shock location ξ_{sh} in inviscid flow

$$\left(\xi_{sh}\right)_{inviscid} = \xi_o \ln (P_o/P_1) \tag{3.7}$$

P_1 is given by Eq. (3.2). The shoulder pressure p_o/H_∞ is shown in carpet plot form in Fig. 3-5. At higher than critical Mach numbers, $M_\infty \geq M_c$, sonic speed is reached before the shoulder expansion and p_o/H_∞ is well approximated by a 90 percent effective Prandtl-Meyer expansion. At lower Mach numbers, $M_\infty < M_c$, the pressure drop through the shoulder expansion remains approximately constant. That is,

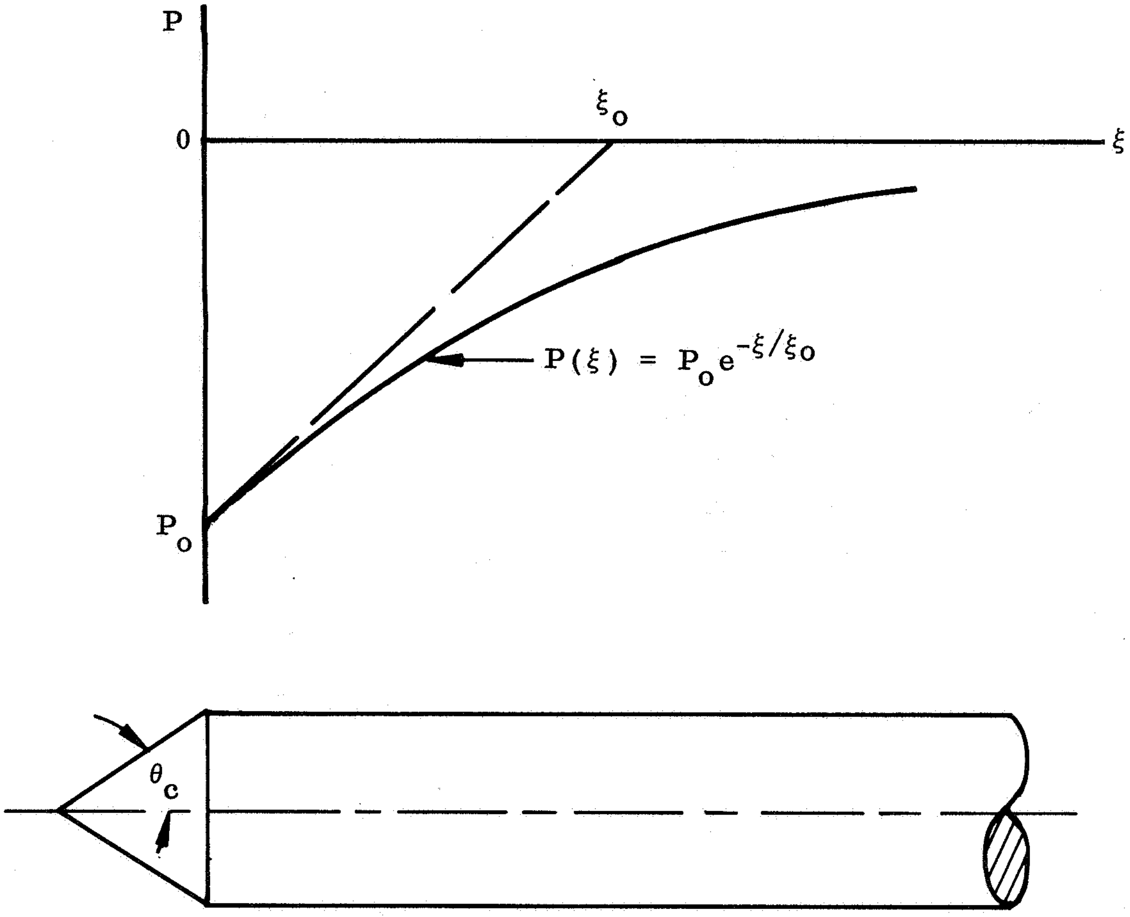

Fig. 3-3 Definition of $P(\xi)$ — Distribution

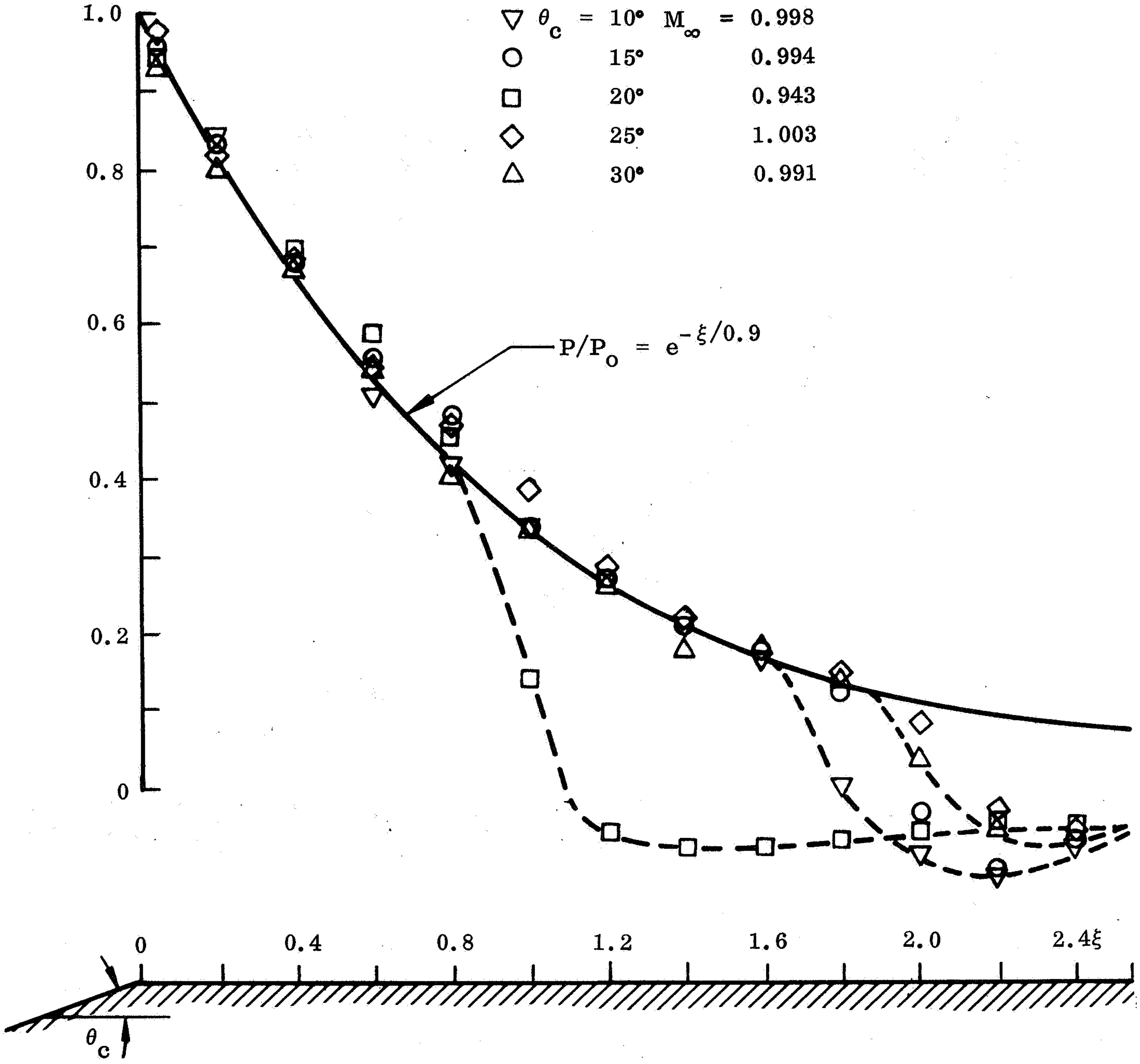

(a) EFFECT OF CONE ANGLE ON PRESSURE DECAY

Fig. 3-4 Pressure Decay $P(\xi)$ From Shoulder Pressure P_o at $\alpha = 0$

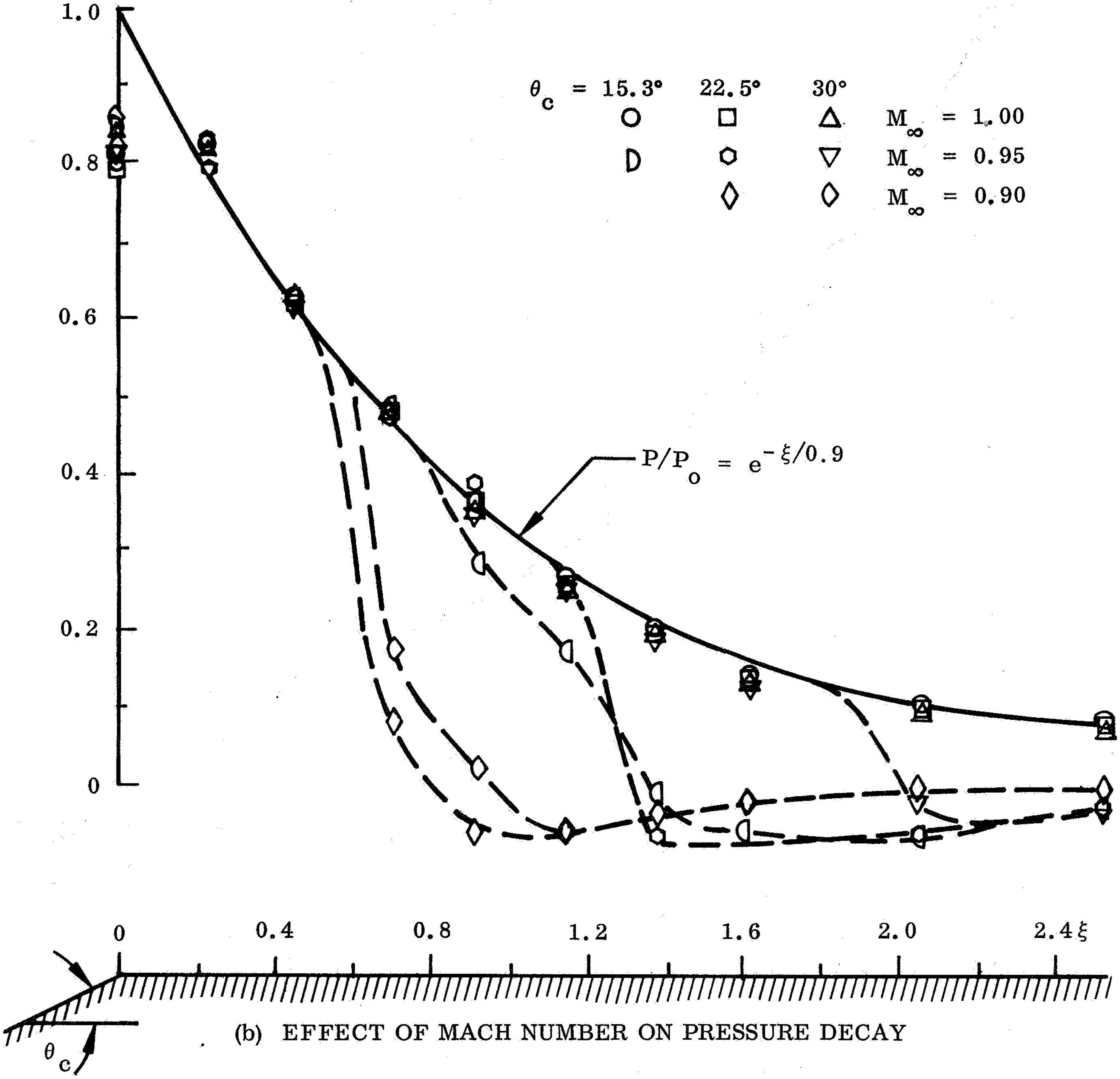

(b) EFFECT OF MACH NUMBER ON PRESSURE DECAY

Fig. 3-4 Pressure Decay P (ξ) From Shoulder Pressure P_o at α = 0 (Cont.)

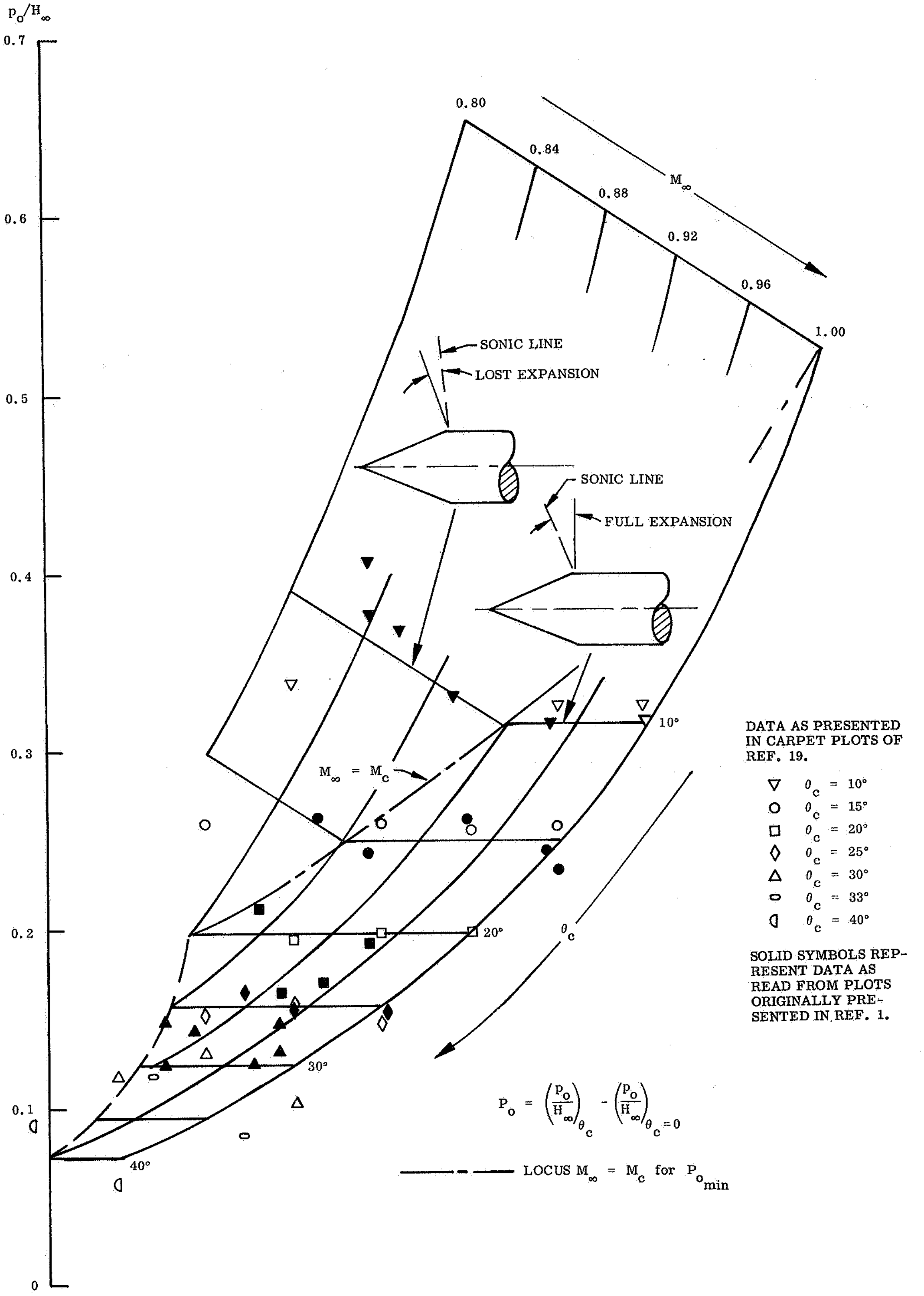

Fig. 3-5 Shoulder Pressure P_o as a Function of Cone Angle θ_c and Mach Number M_∞ at $\alpha = 0$

$$\left.\begin{aligned} P_o &\approx \begin{cases} \left(p_o/H_\infty\right)_{\theta_c} - p_\infty/H_\infty & ; \quad M_\infty \geq M_c \\ \left(P_o\right)_{M_\infty = M_c} & ; \quad M_\infty < M_c \end{cases} \\ \left(p_o/H_\infty\right)_{\theta_c} &= \left(p/H_\infty\right)_{\nu = 0.9\theta_c} \end{aligned}\right\} \qquad (3.8)$$

For the low supersonic range, $1 < M_\infty \leq 2$, the following approximation of p/H_∞ gives less than 3-percent error. (See a coming interim report under the present contract NAS 8-20354.)

$$\left(p/H_\infty\right)_{\nu = 0.9\theta_c} \approx 0.528\, e^{-2.7\theta_c} \qquad (3.8a)$$

With P_o defined by Eq. (3.8), experimental data from Refs. 1 and 8 were plotted in form of $P(\xi)/P_o$ (Fig. 3-4). As can be seen, one value of ξ_o ($\xi_o = 0.9$) in Eq. (3.6) defines the attached flow pressure decay within the scatter of the experimental data.

When the cone-cylinder shoulder is spherically rounded (Ref. 9) the pressure decay is approximately given by Eq. (3.6) if ξ is substituted by $\xi + \Delta\xi_o$, as sketched in Fig. 3-6. That is,

$$P(\xi) \approx P_o\, e^{-(\xi + \Delta\xi_o)/0.9}$$

$$\Delta\xi_o \approx (\Delta\xi_1 + \Delta\xi_2)/2$$

$$= (\sin\theta_c + \operatorname{cosec}\theta_c - \cot\theta_c)\, r_c/2 \qquad (3.9)$$

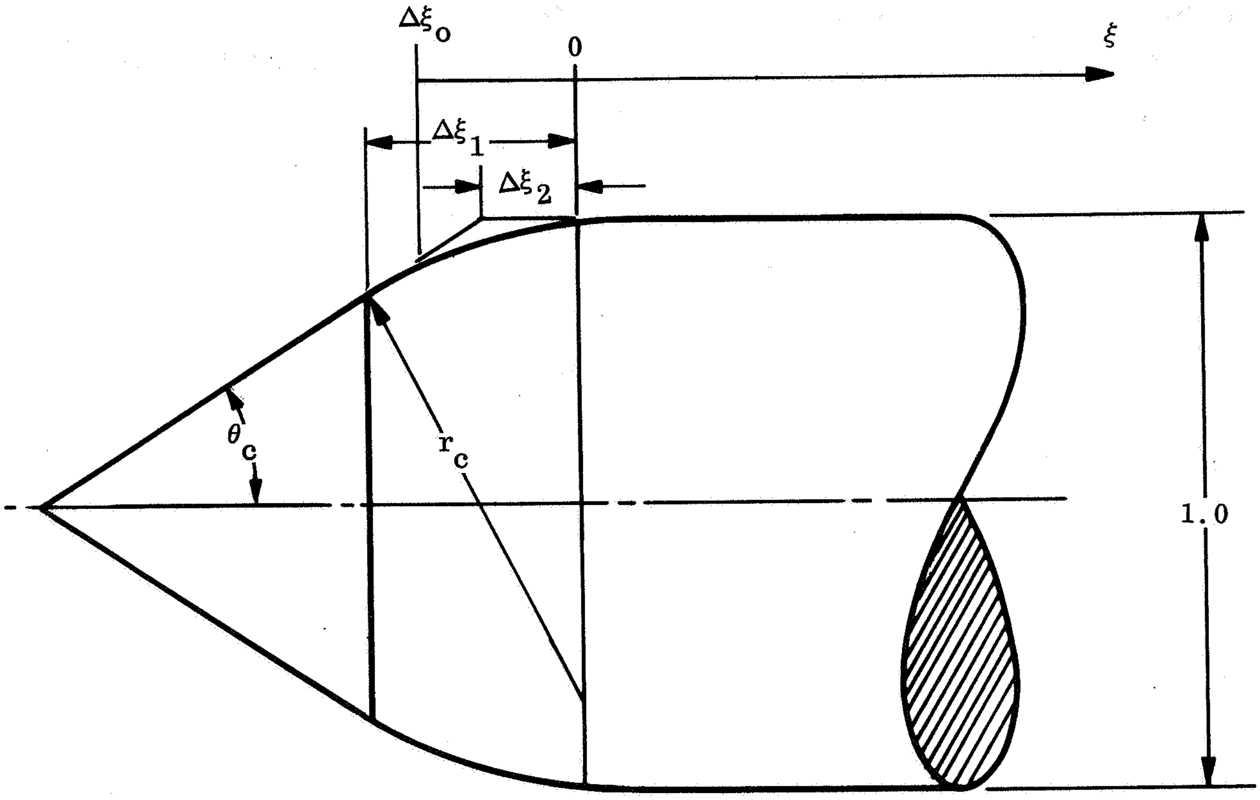

Fig. 3-6 Effective Shoulder for Spherical Shoulder Roundness

The inviscid pressure distributions given by Eqs. (3.6) and (3.8) for sharp shouldered cone-cylinder bodies at $M_\infty = 0.88$ are shown in Fig. 3-7. The steepening adverse pressure gradient with increasing cone angle is amply demonstrated. Combining Eqs. (2.2), (2.7), and (2.8) for $\xi_o = 0.9$ gives the inviscid shock position (Fig. 3-8). In attached flow the boundary-layer displacement thickness slope $\partial\delta^*/\partial x$ would cause the pressure aft of the shock to be p', where $p'/p_\infty > 1$. Assuming a turbulent boundary layer with one-seventh power profile gives (Ref. 10)

$$\left(\frac{\partial\delta^*}{\partial x}\right)_{cyl} = \sqrt{3}\left(\frac{\partial\delta^*}{\partial x}\right)_{\text{Flat Plate}}$$

$$= 0.0392\, R_{e_x}^{-1/7}$$

The tests in Ref. 1 were performed at $R_{e_c} \simeq 0.4 \times 10^6$. The corresponding slope given by the above expression is:

$$p'/p_\infty = \begin{cases} 1.103 & ; \quad \xi = 0.5 \\ 1.096 & ; \quad \xi = 1.0 \\ 1.089 & ; \quad \xi = 2.0 \end{cases}$$

By exponentially decaying the shoulder pressure from p_o to p', the obtained attached flow shock position would be identically the inviscid shock location shown in Fig. 3-8. Because of the boundary-layer shock interaction and attendant local flow separation, the terminal-shock location in viscous flow (Fig. 3-9) is well upstream of the shock position in inviscid flow, as illustrated in Figs. 3-9 and 3-10.

The aerodynamic loads produced by the shock-induced boundary-layer separation are determined solely by the terminal-shock motion along the vehicle. As shown in Appendix B, the separation-induced load can be approximated as follows:

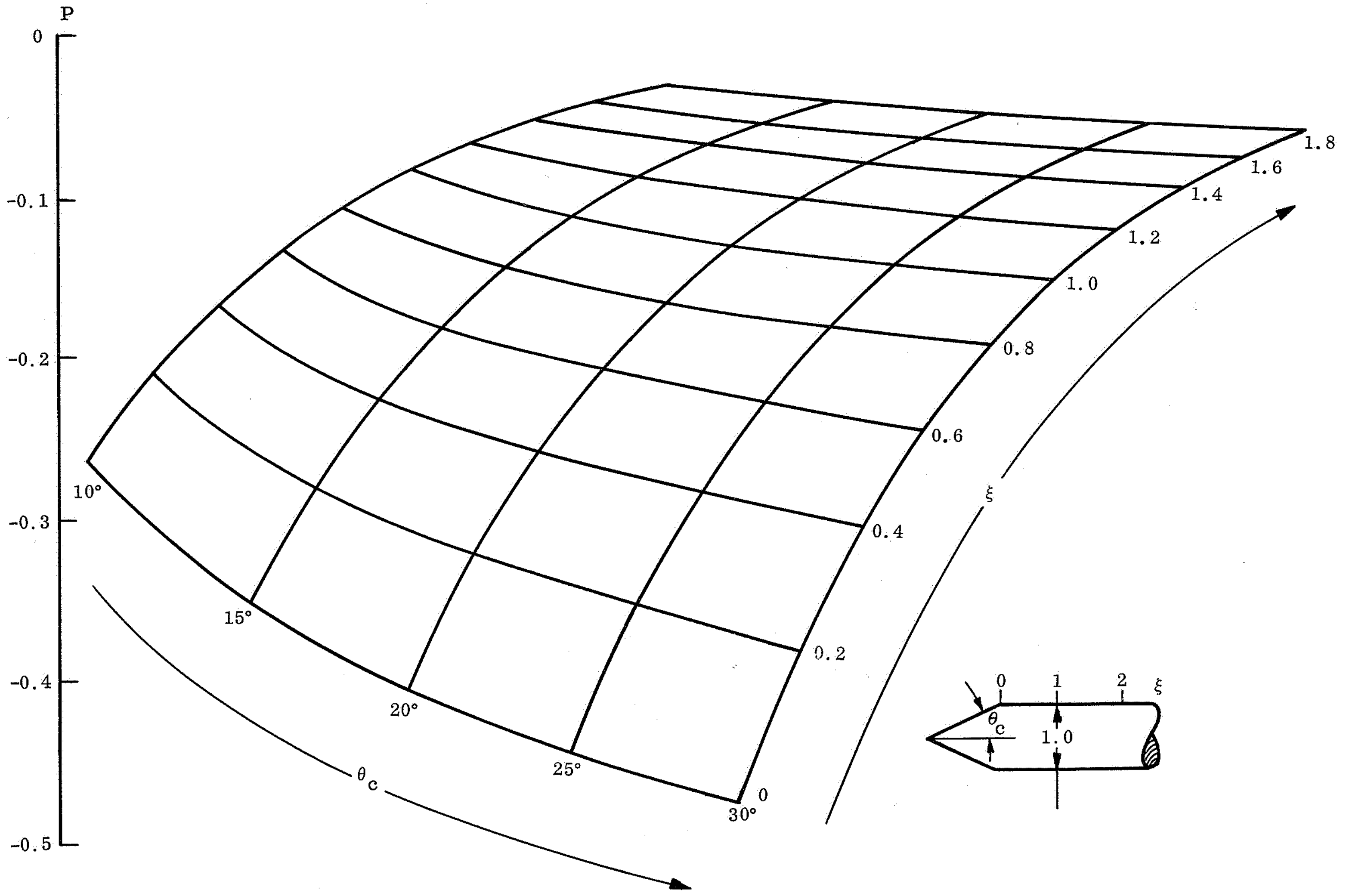

Fig. 3-7 Inviscid Pressure Distribution P (ξ) at M_∞ = 0.88 and α = 0

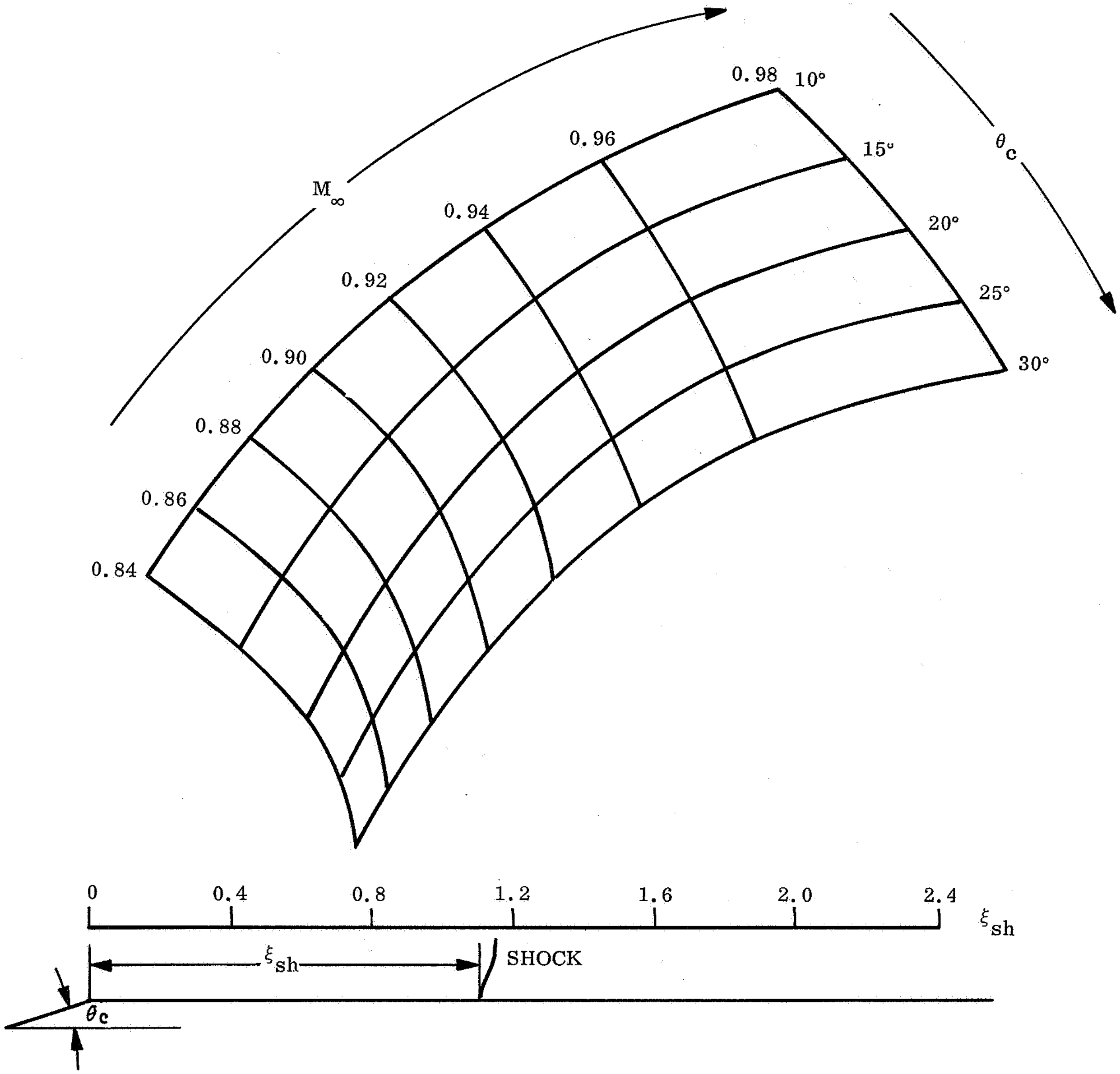

Fig. 3-8 Combined Effect of Mach Number and Cone Angle on the Terminal-Shock Location in Inviscid Flow Over Cone-Cylinder Bodies at $\alpha = 0$

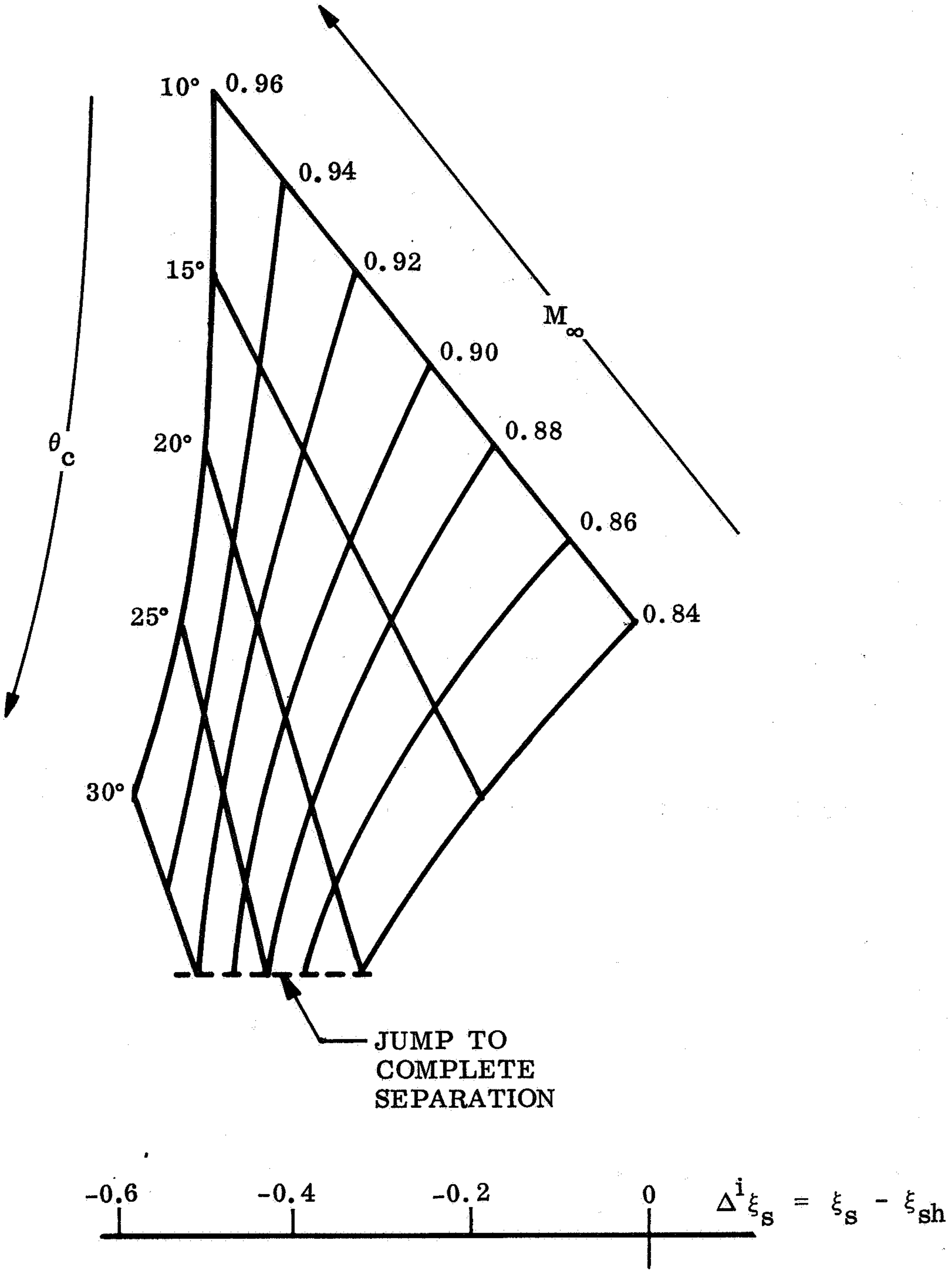

Fig. 3-9 Effect of Boundary Layer on Terminal-Shock Location at $\alpha = 0$

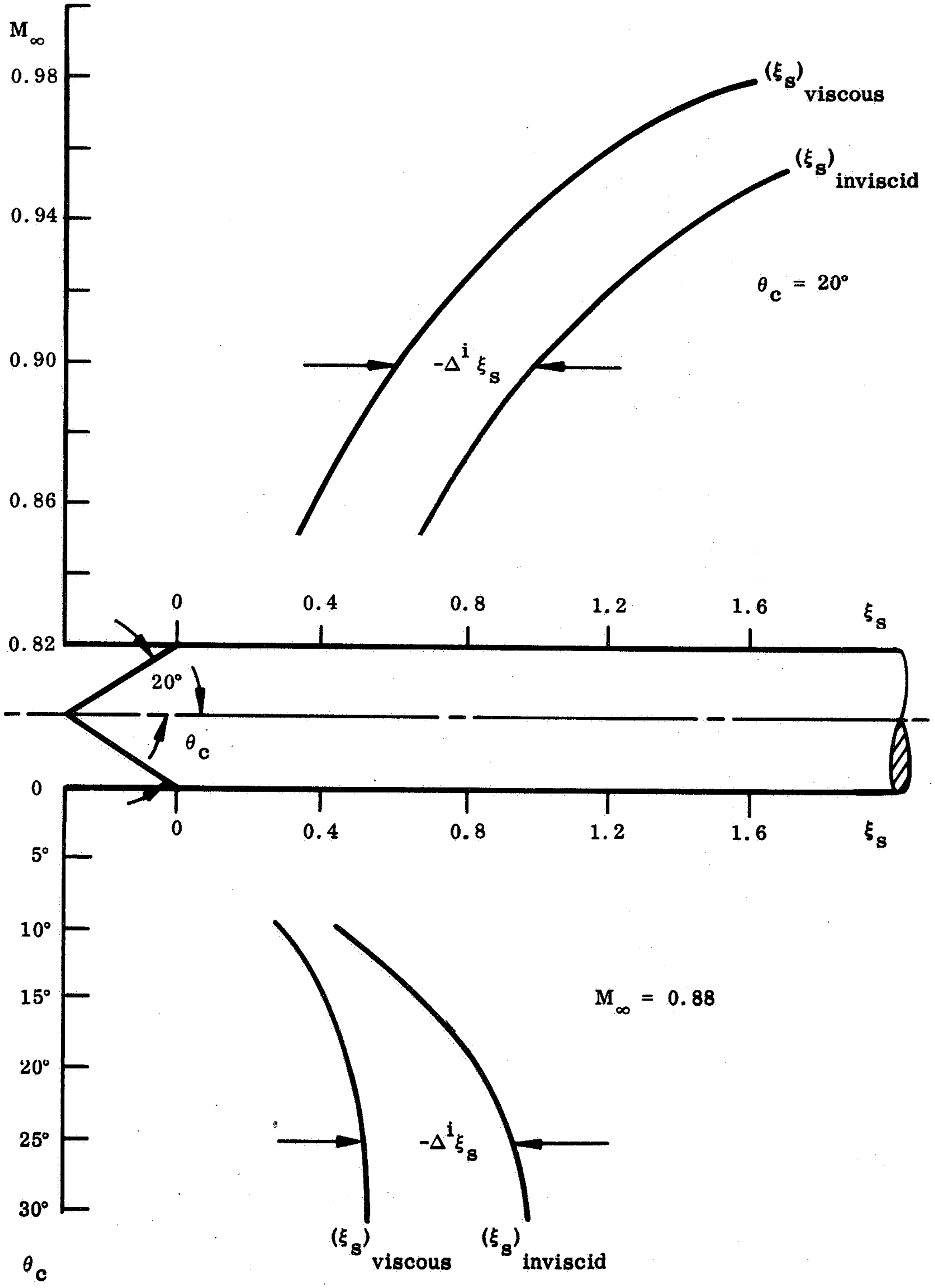

Fig. 3-10 Terminal-Shock Location in Inviscid and Viscous Flow on Cone-Cylinder Bodies at α = 0

$$\Delta^i C_{N_\alpha} = \Delta C_{p_s} \frac{d\Delta^i \xi_s}{d\alpha} \qquad (3.10)$$

where ΔC_{p_s}, the pressure jump across the shock, is a constant. The shock motion derivative $d\Delta^i \xi_s/d\alpha$ is the difference between the viscous and inviscid motion derivatives, $d\Delta^i \xi_s/d\alpha = d\xi_s/d\alpha - d\xi_{sh}/d\alpha$, where $d\xi_s/d\alpha$ is given by static experimental data (Fig. 2-6) and $d\xi_{sh}/d\alpha$ can be computed, Eqs. (3.7) and (3.8). However, the shock position at angle-of-attack is determined by boundary-layer buildup $(d\delta/d\alpha)$ and adverse pressure gradient $(dP/d\xi)$.* Before the shock position in unsteady flow can be determined, one needs to be able to differentiate between these two effects. For constant shock strength (see Appendix B for justification), the following relations exist:

$$\frac{d\Delta^i \xi_s}{d\alpha} = \frac{\partial \Delta^i \xi_s}{\partial \delta} \frac{d\delta}{d\alpha} + \frac{\partial \Delta^i \xi_s}{\partial P_{\xi_s}} \frac{dP_{\xi_s}}{d\alpha} \qquad (3.11)$$

$$\frac{d\delta}{d\alpha} = \frac{\partial \delta}{w_{AC}} \frac{dw_{AC}}{d\alpha} + \frac{\partial \delta}{\partial P_{\xi_s}} \frac{dP_{\xi_s}}{d\alpha}^{**} \qquad (3.12)$$

$$\frac{dP_{\xi_s}}{d\alpha} = \left(\frac{\partial P_{\xi_s}}{\partial \alpha}\right)_\delta + \frac{\partial P_{\xi_s}}{\partial \delta} \frac{d\delta}{d\alpha} \qquad (3.13)$$

---

*$dP/d\xi = (\gamma/2) M_\infty^2 (p_\infty/H_\infty) dC_p/d\xi$

**The last term can be neglected, i.e., $\left(\partial\delta/\partial P_{\xi_s}\right)\left(dP_{\xi_s}/d\alpha\right) = 0$. w_{AC} is the crossflow at the aerodynamic center upstream of the shock position. That is, forebody crossflow effects on boundary-layer buildup are lumped in the manner described in Ref. 4.

When Eqs. (3.11) through (3.13) are combined, the component of $d\Delta^i\xi_s/d\alpha$ due to boundary-layer buildup is obtained:

$$\left(\frac{d\Delta^i\xi_s}{d\alpha}\right)_{B.L.} = \left(\frac{\partial\Delta^i\xi_s}{\partial\delta} + \frac{\partial\Delta^i\xi_s}{\partial P_{\xi_s}}\frac{\partial P_{\xi_s}}{\partial\delta}\right)\frac{\partial\delta}{\partial w_{AC}}\frac{dw_{AC}}{d\alpha} \qquad (3.14)$$

The component due to inviscid pressure gradient increase is

$$\left(\frac{\partial\Delta^i\xi_s}{\partial\alpha}\right)_\delta = \frac{\partial\Delta^i\xi_s}{\partial P_{\xi_s}}\left(\frac{\partial P_{\xi_s}}{\partial\alpha}\right)_\delta \qquad (3.15)$$

In the first approximation, the effect of angle-of-attack without boundary-layer buildup is equivalent to the effect of nose-cone angle (both effects given by a 90-degree effective Prandtl-Meyer expansion), i.e.,

$$\left(\frac{\partial\Delta^i\xi_s}{\partial\alpha}\right)_\delta = \frac{d\Delta^i\xi_s}{d\theta_c} = \frac{d\xi_s}{d\theta_c} - \frac{d\xi_{sh}}{d\theta_c} \qquad (3.16)$$

The boundary-layer buildup effect makes up the rest of the total angle-of-attack effect, as illustrated in Fig. 3-11. When the shock moves closer to the cone-cylinder shoulder with decreasing M_∞, the effect of the boundary-layer buildup, $(d\Delta^i\xi_s/d\alpha)_{B.L.}$, decreases. This is the result of the decreased forebody length. Only the portion aft of the shoulder is effective in this buildup, since the shoulder essentially serves as the starting point for a new boundary layer with or without reverse transition from turbulent to laminar boundary layer (Ref. 11). At $M_\infty = 0.85$, the boundary-layer buildup effect has disappeared for 20° cone angle (Fig. 3-11). The force derivative

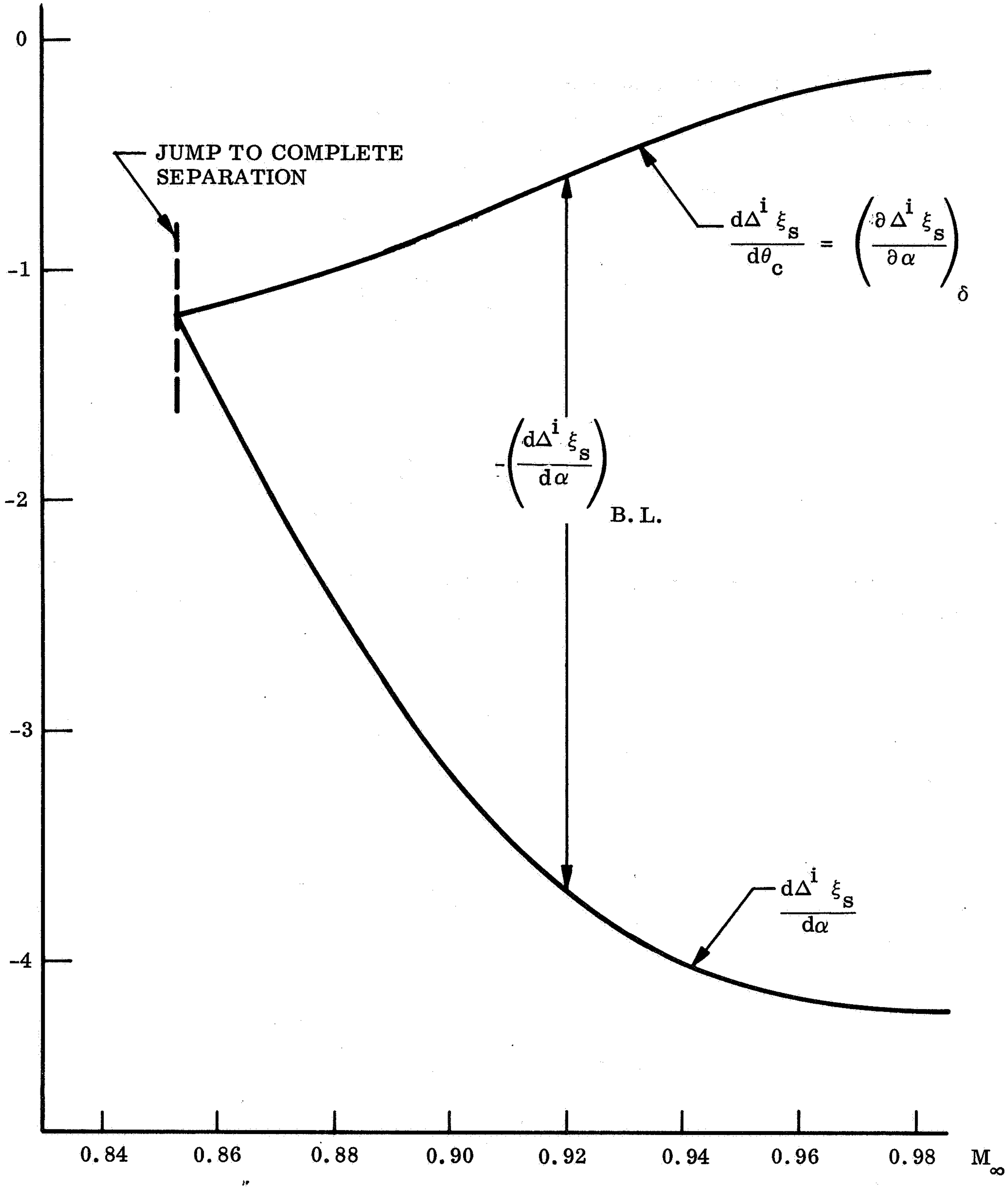

Fig. 3-11 Effect of Boundary-Layer Thickness and Pressure Gradient on the Terminal-Shock Movement on a 20° Cone-Cylinder Body at $\alpha = 0$ and High Subsonic Mach Numbers

induced by this shock movement is shown in Fig. 3-12, as obtained by use of the shock pressure jump, shown by Fig. 2-4 and Eq. (3.10).*

The two force components are

$$\left(\frac{\partial \Delta^i C_N}{\partial \alpha}\right)_\delta = \Delta C_{p_s} \left(\frac{\partial \Delta^i \xi_s}{\partial \alpha}\right)_\delta \tag{3.17}$$

$$\left(\frac{d\Delta^i C_N}{d\alpha}\right)_{B.L.} = \Delta C_{p_s} \left(\frac{d\Delta^i \xi_s}{d\alpha}\right)_{B.L.} \tag{3.18}$$

The pressure gradient immediately ahead of the point of separation (ξ_s), given by Eq. (3.6), is

$$P_{\xi_s} = - \left(\frac{\partial P}{\partial \xi}\right)_s = - \frac{P_s}{\xi_o} \tag{3.19}$$

Thus,

$$\left(\frac{\partial P_{\xi_s}}{\partial \theta_c}\right)_{\text{inviscid}} = - \frac{P_s}{P_o} \frac{\partial P_o}{\partial \theta_c} \Big/ \xi_o$$

$$\left(\frac{\partial P_{\xi_s}}{\partial \alpha}\right)_{\text{inviscid}} = - \frac{P_s}{P_o} \frac{\partial P_o}{\partial \alpha} \Big/ \xi_o \tag{3.20}$$

---

*The preliminary data used in Appendix C of Ref. 12 and in Ref. 13 deviate somewhat from the more accurate data shown in Figs. 3-11 through 3-14 of this report.

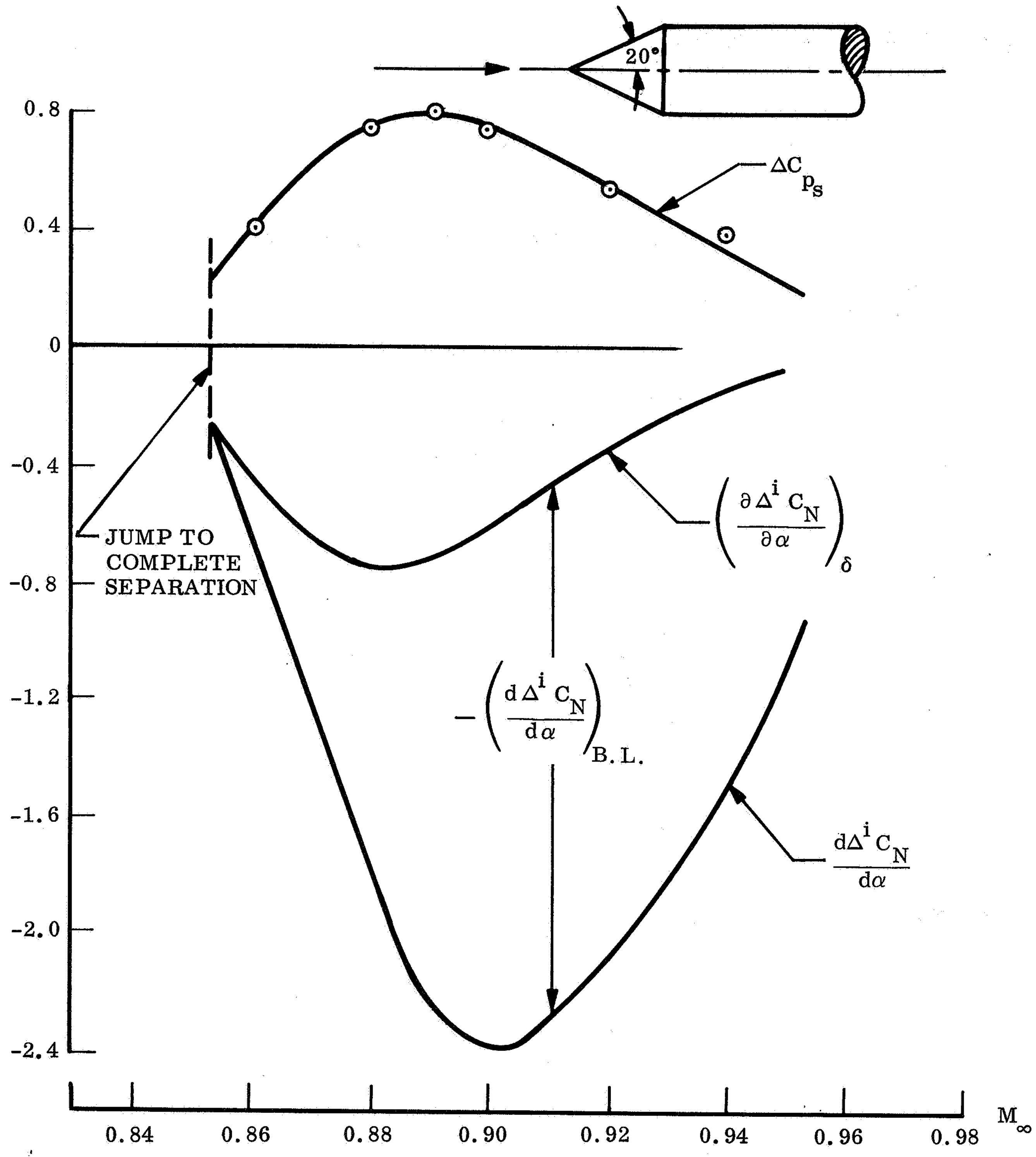

Fig. 3-12 Normal Force Derivatives Induced by the Terminal-Shock Movement on a 20° Cone-Cylinder Body at $\alpha = 0$ and High Subsonic Mach Numbers

Equations (3.8) and (3.8a) give

$$\frac{\partial P_o}{\partial \theta_c} = -\,2.7\,p_o/H_\infty \tag{3.21}$$

Assuming as before that $\left(\partial P_o/\partial \alpha\right)_\delta$ is given by $\partial P_o/\partial \theta_c$, one obtains $\left(\partial P_{\xi_s}/\partial \alpha\right)_{\text{inviscid}} = \left(\partial P_{\xi_s}/\partial \alpha\right)_\delta$ as follows:

$$\left(\frac{\partial P_{\xi_s}}{\partial \alpha}\right)_\delta = 2.7\,\frac{P_s}{P_o}\,\frac{p_o}{H_\infty}\Big/\xi_o \tag{3.22}$$

where

$$\frac{P_s}{P_o} = \frac{C_{p_s}}{C_{p_o}} \approx -\,\frac{\Delta C_{p_s}}{C_{p_{min}}}$$

$$\frac{p_o}{H_\infty} = 0.528\,e^{-2.7\,\theta_c}$$

Also, from Eq. (3.6),

$$\frac{P_s}{P_o} = e^{-\xi_s/\xi_o}$$

where

$$\xi_o = 0.9.$$

Hence,

$$\left(\frac{\partial P_{\xi_s}}{\partial \alpha}\right)_{\delta} = 1.584\, e^{-(1.11\,\xi_s + 2.7\,\theta_c)} \qquad (3.23)$$

The measured total $dP_{\xi_s}\ d\alpha$ may be determined as (see sketch in Fig. 3-13)

$$\frac{dP_{\xi_s}}{d\alpha} = P_{\xi_s}\, \frac{dC_{p_s}}{d\alpha} \Big/ C_{p_s} \qquad (3.24)$$

where

$$P_{\xi_s} = -\frac{P_s}{P_o}\,\frac{P_o}{\xi_o} = -\,1.11\, e^{-1.11\,\xi_s}$$

For high cone angles θ_c, the measured effect of angle-of-attack approaches the estimated effect for constant boundary layer (Fig. 3-13). However, for more slender nose cones, the boundary-layer buildup effect, $\left(dP_{\xi_s}/d\alpha\right)_{B.L.}$, has an alleviating influence that at $\theta_c = 15°$ is large enough to cancel completely the inviscid pressure gradient increase with α. Thus, the boundary-layer buildup effect $\left(d\Delta^i\xi_s/d\alpha\right)_{B.L.}$ peaks out at $\theta_c = 20°$ (Fig. 3-14). At lower θ_c, it decreases because of the increased $\left(dP_{\xi_s}/d\alpha\right)_{B.L.} = \left(\partial P_{\xi_s}/\partial\delta\right)\ (d\delta/d\alpha)$; at higher θ_c, it decreases because the decreasing magnitude of $\left(\partial\Delta^i{}_{\xi_s}/\partial\delta\right)\ (d\delta/d\alpha)$, resulting when the shock moves closer to the shoulder (as noted earlier in discussing Fig. 3-11). With $\left(\partial\Delta^i{}_{\xi_s}/\partial\alpha\right)_{\delta}$ measured as $\left(d\Delta^i{}_{\xi_s}/d\theta_c\right)$, and $\left(\partial P_{\xi_s}/\partial\alpha\right)_{\delta}$ predicted by Eq. (3.23), the effect of inviscid pressure gradient, $\partial\Delta^i\xi_s/\partial P_{\xi_s}$, is given by Eq. (3.15). The results for $M_\infty = 0.88$ are shown in Fig. 3-15.

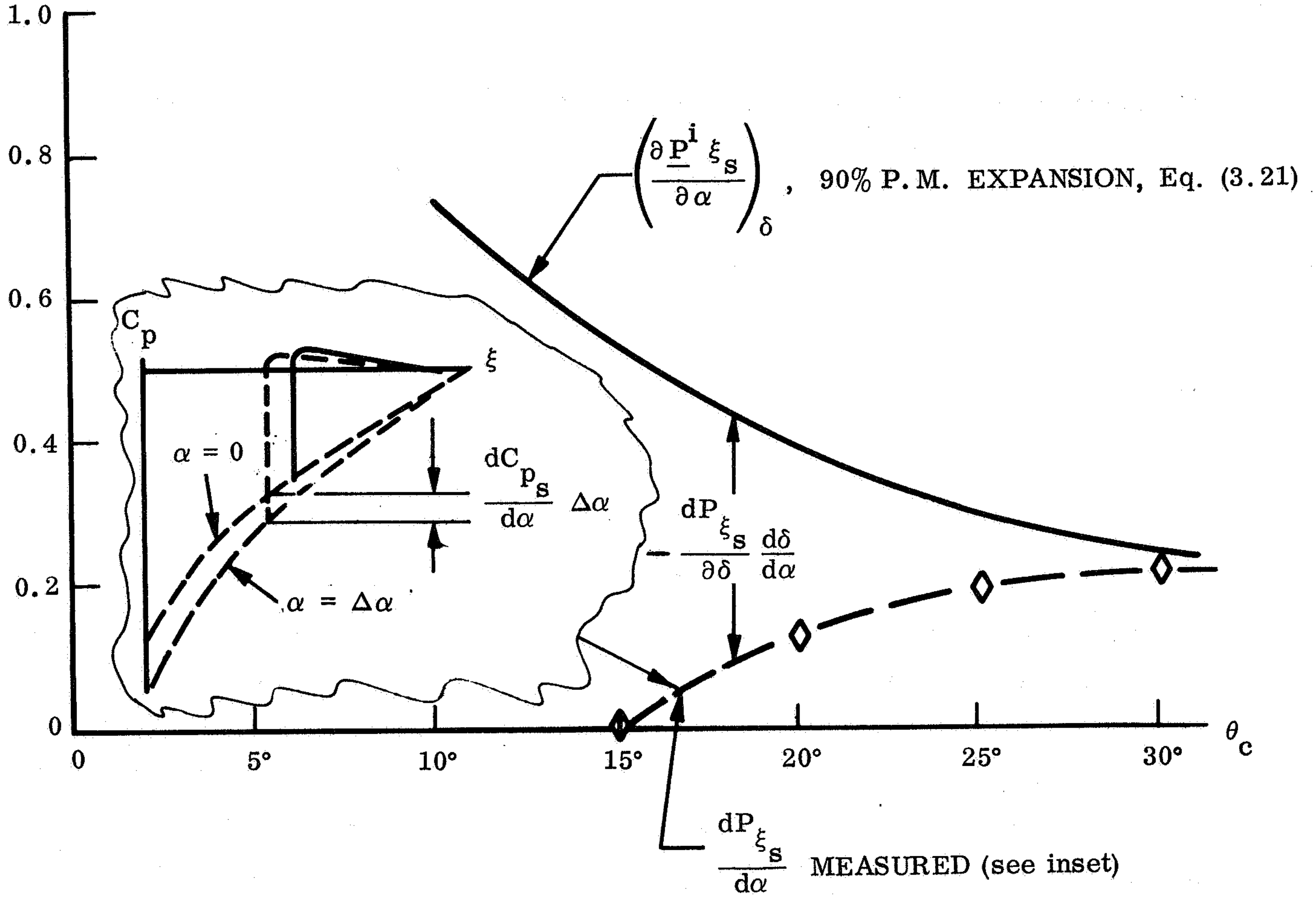

Fig. 3-13 Effect of Angle-of-Attack on Adverse Pressure Gradient Around $\alpha = 0$ at $M_\infty = 0.88$

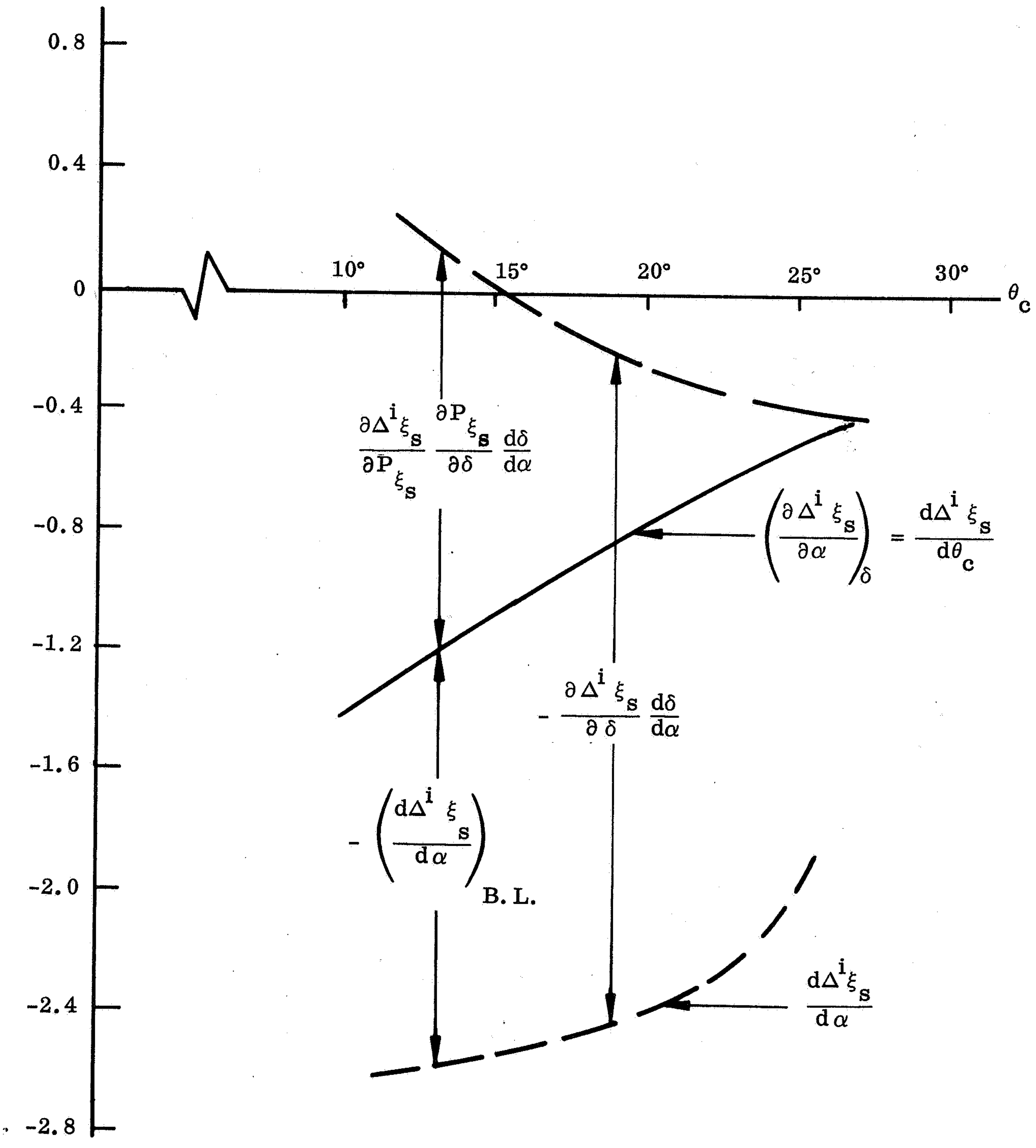

Fig. 3-14 Breakdown of the Angle-of-Attack Effect $d\Delta^i\xi_s/d\alpha$ Into its Various Components at $\alpha = 0$ and $M_\infty = 0.88$

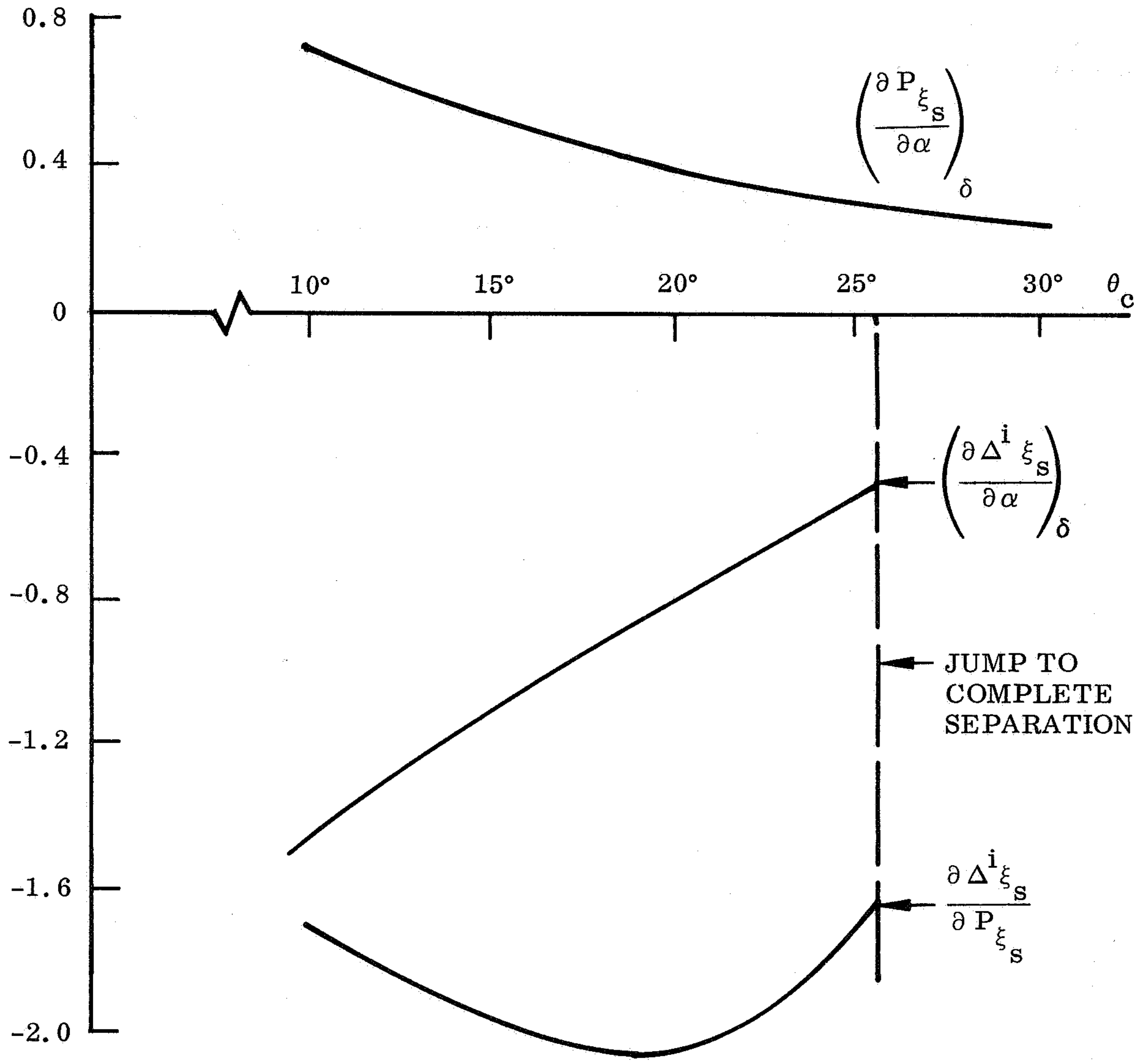

Fig. 3-15 Effects of Inviscid Pressure Gradient at $\alpha = 0$ and $M_\infty = 0.88$

When the shock approaches the cone-cylinder shoulder, it will suddenly jump all the way forward to the shoulder and complete flow separation occurs. The cause is the weakening boundary-layer profile resulting from the very steep adverse pressure gradient at the shoulder. This is well illustrated by use of the boundary-layer shape parameter, as was done by Robertson and Chevalier (Ref. 1 and Fig. 3-16). The 30° cone-cylinder illustrates how the leeward side on the 20° cone-cylinder would appear at a moderate angle-of-attack. Further research by Robertson and Chevalier (Ref. 14) revealed that the flow could alternate between retarded shock-induced separation and complete separation. Their results, shown in Fig. 3-17, indicate that this jump from one flow condition to another could occur for a fixed model (within sting stiffness limitations) in a large $M_\infty - \alpha$ region. For the blunter nose cones, only the windward side had this alternating flow; on the slender 15° cone-cylinder body, only the leeward side had it.

3.3 UNSTEADY TERMINAL-SHOCK AERODYNAMICS

The pressure gradient of the external flow at the edge of the boundary layer is given by the complete Bernoulli equation

$$-\frac{1}{\rho_e}\frac{\partial p_e}{\partial x_1} = \frac{\partial U_e}{\partial t} + U_e \frac{\partial U_e}{\partial x_1} \tag{3.25}$$

Or with $\xi = \frac{x_1}{c}$ (c = reference length, e.g. cylinder caliber)

$$\frac{\partial p_e}{\partial \xi} = -\rho_e U_e \left[\frac{\partial U_e}{\partial t}\frac{c}{U_e} + \frac{\partial U_e}{\partial \xi} \right] \tag{3.26}$$

For constant vehicle velocity, U_e changes only through body pitching or bending. Thus, with $p_e = p$

$$\frac{\partial p}{\partial \xi} = -\rho_e U_e \left[\frac{\partial U_e}{\partial \alpha}\frac{c\dot{\alpha}}{U_e} + \frac{\partial U_e}{\partial \xi} \right] \tag{3.27}$$

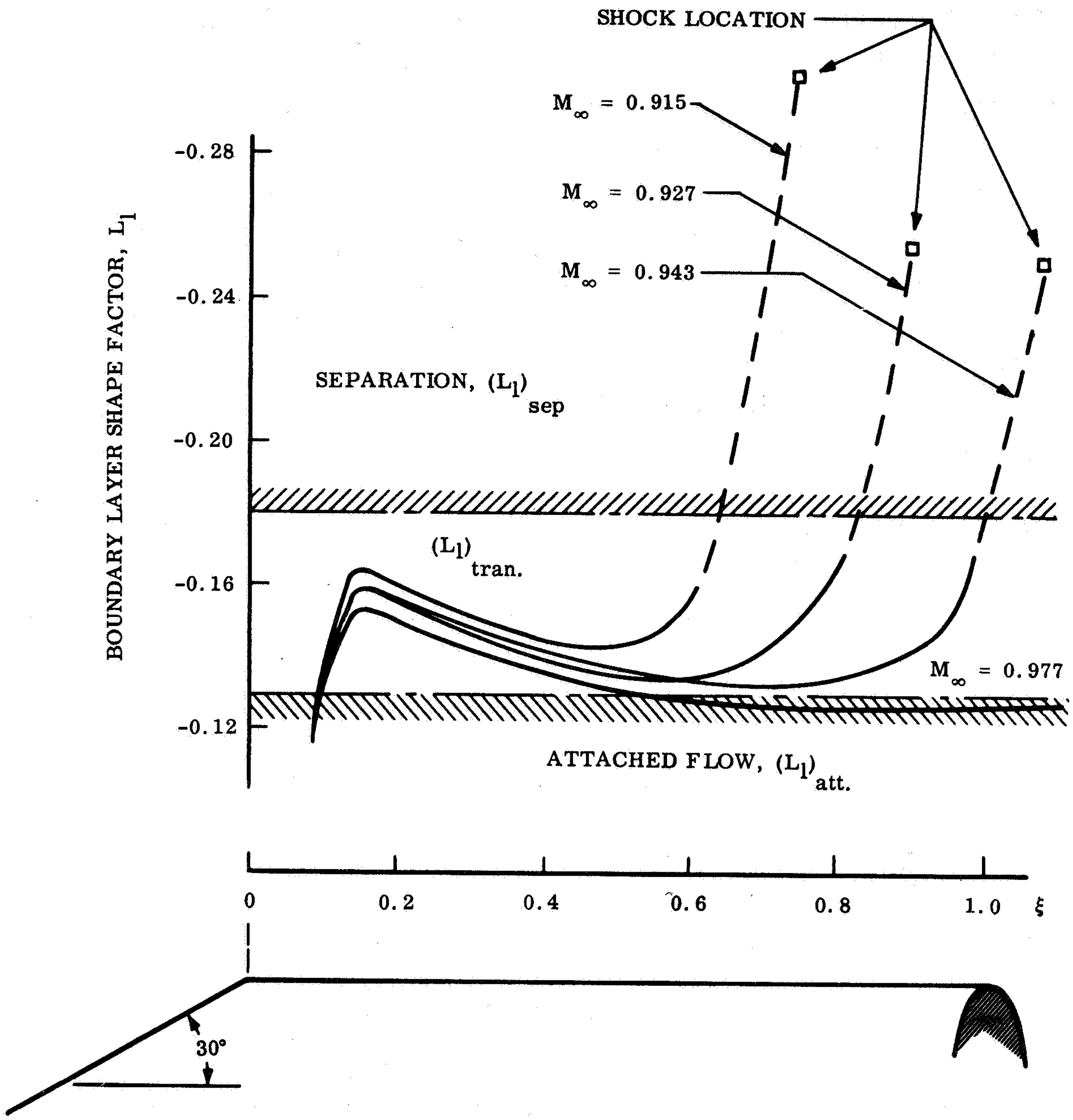

Fig. 3-16 Axial Variation of the Boundary-Layer Auxiliary Shape Factor on a 30° Cone-Cylinder Body at $\alpha = 0$ and Various Mach Numbers

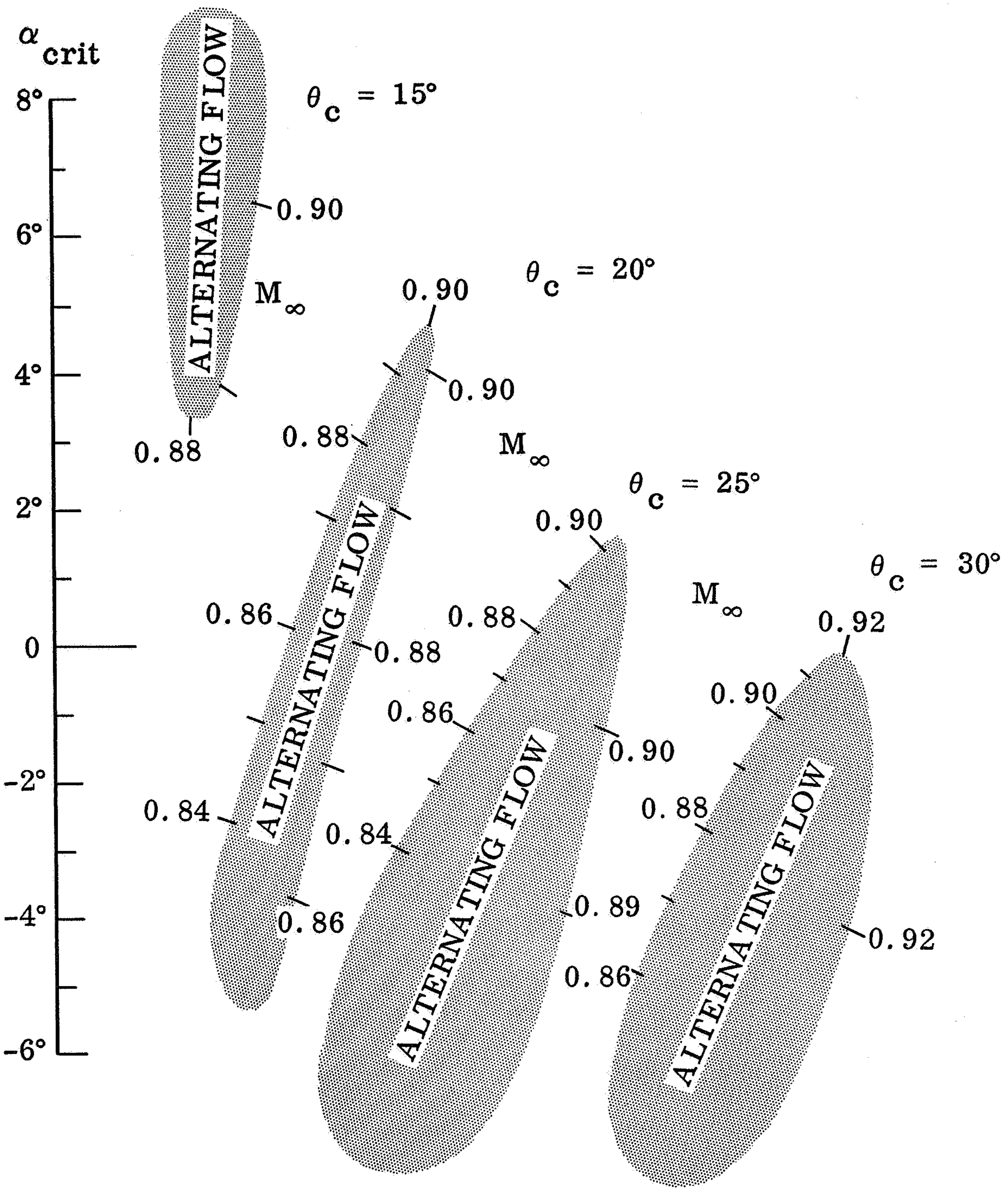

Fig. 3-17 α-M_∞-Regions for Fluctuating Flow on Cone-Cylinder Bodies With Various Cone Half-Angles

That is,

$$\frac{\partial p}{\partial \xi} = \left(\frac{\partial p}{\partial \xi}\right)_{\dot{\alpha}=0} + \frac{\partial p}{\partial \alpha} \cdot \frac{c\dot{\alpha}}{U_e} \tag{3.28}$$

Equation (3.28) is also valid for $P_s = (p_s/H_\infty) - (p_\infty/H_\infty)$ and gives, together with Eq. (3.6),

$$\frac{\partial P_s}{\partial \xi} = \left(\frac{\partial P_s}{\partial \xi}\right)_{\dot{\alpha}=0} + \frac{P(\xi_s)}{P_o} \frac{\partial P_o}{\partial \alpha} \frac{c\dot{\alpha}}{U_e} \tag{3.29}$$

where $(\partial P_o/\partial \alpha)$ for supercritical Mach numbers, $M_\infty > M_c$, is defined by a 90-percent effective Prandtl-Meyer expansion,

$$\left(\frac{\partial P_o}{\partial \alpha}\right)_{M_\infty > M_c} = 0.9 \frac{p_\infty}{H_\infty} \frac{\partial}{\partial \nu} \left(\frac{p}{p_\infty}\right) \tag{3.30}$$

By use of Eq. (3.8a), $\partial P_o/\partial \alpha$ can be approximated as

$$\left.\begin{aligned} \frac{\partial P_o}{\partial \alpha} &= -1.43\, e^{-2.7\alpha} \quad ; \quad M_\infty > M_c \\ \frac{\partial P_o}{\partial \alpha} &= 0 \quad ; \quad M_\infty \le M_c \end{aligned}\right\} \tag{3.31}$$

The critical Mach number M_c is given in Fig. 3-5 as a function of cone angle θ_c. It is apparent that only for $M_\infty > M_c$ will the jump to complete separation occur. Hence, only $M_\infty > M_c$ is of interest and will be assumed for the remainder of the analysis. It should be emphasized that for $\theta_c = 15°$, for example, the leeward-side effective cone angle is equivalent to $\theta_c + \alpha$; and when the leeward-side jump to complete separation occurs for 6° $< \alpha <$ 8° (Fig. 2-2), the shoulder expansion takes place at a supercritical (local) Mach number.

Equations (3.29) through (3.31) show that body pitching (or bending) motion, $(c\dot{\alpha}/U_e) > 0$, will decrease the pressure gradient $\partial P_s/\partial \xi$ and will, therefore, delay the boundary-layer separation. That is, the separation will in the unsteady case lag behind its static or steady-state position. This lag, added to the lag in the boundary-layer buildup, makes the separation have opposite effects on static and dynamic stability and accounts for the sometimes drastic effect of flow separation on vehicle dynamics.

Quasi-steady methods are used to compute unsteady characteristics by use of experimental static characteristics (Ref. 4). The treatment of the boundary-layer buildup effect in Ref. 4 is directly applicable to the present case. The quasi-steady means that accounts for the accelerated flow effect will be derived.

Generally, the separation-induced loading is determined solely by the shock motion. The shock strength remains constant within the approximations used here to compute first-order effects of the shock perturbations. The load $\Delta^i C_N$ may, of course, be distributed more realistically around ξ_s rather than be considered a point load. The effect of body pitching on the external flow pressure gradient is given by Eqs. (3.29) through (3.31). If the static force induced by a change in the pressure gradient were known, the unsteady force induced through the accelerated flow effect could be computed also. That is,

$$\Delta^i C_N \left(P_{\xi_s}\right) = \frac{\partial \Delta^i C_N}{\partial P_{\xi_s}} \, \frac{\partial P_{\xi_s}}{\partial \dfrac{c\dot{\alpha}}{U_e}} \, \frac{c\dot{\alpha}}{U_e} \qquad (3.32)$$

where, from Eq. (3.29),

$$\frac{\partial P\xi_s}{\partial \frac{c\dot{\alpha}}{U_e}} = \frac{P(\xi_s)}{P_o}\,\frac{\partial P_o}{\partial \alpha} \tag{3.33}$$

Combining Eqs. (3.6), (3.31), and (3.33) gives

$$\frac{\partial P_{\xi_s}}{\partial \frac{c\dot{\alpha}}{U_e}} = 1.43\, e^{-(1.11\,\xi_s + 2.7\alpha)} \tag{3.34}$$

$\Delta^i C_N$ results from the shock pressure increase ΔC_{p_s} acting over the projected area and is simply (see Appendix B)

$$\frac{\partial \Delta^i C_N}{\partial P_{\xi_s}} = \Delta C_{p_s}\,\frac{\partial \Delta^i \xi_s}{\partial P_{\xi_s}} \tag{3.35}$$

How $\partial \Delta^i \xi_s / \partial P_{\xi_s}$ can be obtained from static data was discussed earlier (in conjunction with Fig. 3-15).

If the cone-cylinder body is describing pitch oscillations, $\theta(t)$, around a certain trim angle-of-attack, α_o, the motion of the terminal shock can be described as follows, using quasi-steady methodology. (See Fig. 3-18.)

With $U(M_\infty)$ constant,

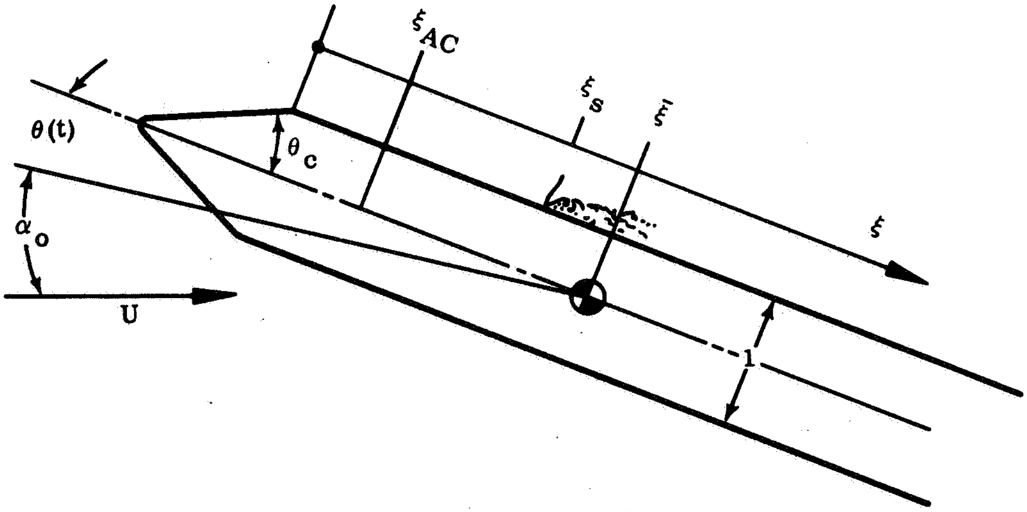

Fig. 3-18 Coordinate Systems

$$\xi_s(t) = \xi_s(\alpha_o) + (\xi_s)_{\text{inv.}}\left(\alpha_o + \theta(t)\right) + \Delta^i\xi_s(t)$$

$$\Delta^i\xi_s(t) = \left(\frac{d\Delta^i\xi_s}{d\alpha}\right)_{\text{B.L.}} \cdot \tilde{\alpha}_{AC}(t - \Delta t) + \left(\frac{\partial\Delta^i\xi_s}{\partial(P_\xi)_s}\right)_\delta \left[\left(\frac{\partial(P_\xi)_s}{\partial\alpha}\right)_\delta \cdot \tilde{\alpha}_s(t) + \left(\frac{\partial P_s}{\partial\alpha}\right)_\delta \frac{c\dot{\theta}}{(U_e)_s}\right]^* \tag{3.36}$$

$$\left.\begin{aligned} \tilde{\alpha}_{AC}(t - \Delta t) &= \theta(t - \Delta t) + (\xi_{AC} - \bar{\xi})\,\frac{c\dot{\theta}(t - \Delta t)}{U} \\ \tilde{\alpha}_s(t) &= \theta(t) + (\xi_s - \bar{\xi})\,\frac{c\dot{\theta}(t)}{U} \end{aligned}\right\} \tag{3.37}$$

For slow oscillations,

$$\begin{aligned} \tilde{\alpha}_{AC}(t - \Delta t) &= \theta(t) - \Delta t\,\dot{\theta}(t) + (\xi_{AC} - \bar{\xi})\,\frac{c\dot{\theta}(t)}{U} \\ &= \theta - \left(\frac{U\Delta t}{c} + \bar{\xi} - \xi_{AC}\right)\frac{c\dot{\theta}}{U} \end{aligned} \tag{3.38}$$

$$\Delta t = (\xi_s - \xi_{AC})\,c/\bar{U}$$

where $\bar{U}$ is the convection velocity in a turbulent boundary layer at subsonic and transonic speeds ($0.8U \le \bar{U} \le U$, Ref. 15). Thus Eq. (3.36) becomes

---

*Only $\Delta^i\xi_s(t)$ is of interest here, since the inviscid shock position is assumed to adjust instantaneously to θ, and can be included in the attached flow characteristics.

$$\Delta^i \xi_s(t) = \left(\frac{d\Delta^i \xi_s}{d\alpha}\right)_{B.L.} \left\{\theta - \left[\frac{U}{\bar{U}}\,(\xi_s - \xi_{AC}) + \bar{\xi} - \xi_{AC}\right]\frac{c\dot{\theta}}{U}\right\}$$

$$+ \left(\frac{\partial \Delta^i \xi_s}{\partial P_{\xi_s}}\right)_{\delta} \left\{\left(\frac{\partial P_{\xi_s}}{\partial \alpha}\right)_{\delta} \left[\theta + (\xi_s - \bar{\xi})\,\frac{c\dot{\theta}}{U}\right] + \left(\frac{\partial P_s}{\partial \alpha}\right)_{\delta} \frac{U}{(U_e)_s}\,\frac{c\dot{\theta}}{U}\right\} \qquad (3.39)$$

$$\frac{\partial \Delta^i \xi_s}{\partial \frac{c\dot{\theta}}{U}} = \Delta^i \xi_{s_{\dot{\theta}}} = -\left(\frac{d\Delta^i \xi_s}{d\alpha}\right)_{B.L.} \left[\frac{U}{\bar{U}}\,(\xi_s - \xi_{AC}) + \bar{\xi} - \xi_{AC}\right]$$

$$+ \left(\frac{\partial \Delta^i \xi_s}{\partial P_{\xi_s}}\right)_{\delta} \left[\left(\frac{\partial P_{\xi_s}}{\partial \alpha}\right)_{\delta} (\xi_s - \bar{\xi}) + \left(\frac{\partial P_s}{\partial \alpha}\right)_{\delta} \frac{U}{(U_e)_s}\right] \qquad (3.40)$$

$$\Delta^i C_{N_{\dot{\theta}}} = \Delta C_{p_s} \cdot \Delta^i \xi_{s_{\dot{\theta}}} \qquad (3.41)$$

When the adverse pressure gradient at the intended shock position exceeds a critical value, the shock jumps all the way to the cone shoulder. The critical value can be expressed in the following form:

In the static case,

$$\left(\frac{dP_s}{d\xi}\right)_{crit} = P_{\xi_s}\,(\alpha_{crit}) \qquad (3.42)$$

In the unsteady case, a higher angle-of-attack, $\alpha_{crit} + \Delta_P \alpha_{crit}$, can be reached because of the delaying effect of flow acceleration on the pressure gradient, and

$$\left(\frac{dP_s}{d\xi}\right)_{crit} = P_{\xi_s}(\alpha_{crit}) + \left(\frac{\partial P_{\xi_s}}{\partial\alpha}\right)_\delta \Delta_p\alpha_{crit} + \left(\frac{\partial P_{\xi_s}}{\partial\alpha}\right)_\delta (\xi_s - \bar{\xi})\frac{c\dot{\theta}}{U} + \left(\frac{\partial P_s}{\partial\alpha}\right)_\delta \frac{c\dot{\theta}}{(U_e)_s} \tag{3.43}$$

That is,

$$\Delta_P\,\alpha_{crit} = \left[\bar{\xi} - \xi_s - \frac{\left(\frac{\partial P_s}{\partial\alpha}\right)_\delta}{\left(\frac{\partial P_{\xi_s}}{\partial\alpha}\right)_\delta}\,\frac{U}{(U_e)_s}\right]\frac{c\dot{\theta}}{U} \tag{3.44}$$

For the blunter nose shapes, this comprises all the delay, since the δ-effect goes to zero near the nose (Fig. 3-11). For more slender nose shapes, however, the boundary-layer buildup also has a delaying effect. If it were solely responsible for the jump to complete separation, the delay for the pitching body would be determined simply by the time lag Δt in the boundary-layer buildup. That is,

$$(\delta_s)_{crit} = \delta(\alpha_o) + \frac{d\delta}{d\alpha}\cdot\alpha_{AC}(t - \Delta t) \tag{3.45}$$

where

$$\Delta t = \frac{U}{\bar{U}}(\xi_s - \xi_{AC})\,c/U$$

That is,

$$\Delta_{B.L.}\,\alpha_{crit} = \left[\frac{U}{\bar{U}}\,(\xi_s - \xi_{AC}) + \bar{\xi} - \xi_{AC}\right]\frac{c\dot{\theta}}{U} \tag{3.46}$$

Using the shock motion sensitivity to boundary-layer buildup and P_{ξ}-changes (Fig. 3-11) as a guide, the total delay $\Delta\alpha_{crit}$ may be expressed as follows:

$$\Delta\,\alpha_{crit} = \frac{\left(\dfrac{\partial\Delta^i\xi_s}{\partial\alpha}\right)_{\delta}}{\dfrac{d\Delta^i\xi_s}{d\alpha}}\,\Delta_p\,\alpha_{crit} + \frac{\left(\dfrac{d\Delta^i\xi_s}{d\alpha}\right)_{B.L.}}{\dfrac{d\Delta^i\xi_s}{d\alpha}}\,\Delta_{B.L.}\,\alpha_{crit} \tag{3.47}$$

and through Eqs. (3.44) and (3.46),

$$\Delta\alpha_{crit} = \left\{\left[\frac{U}{\bar{U}}\,(\xi_s - \xi_{AC}) + \xi - \xi_{AC}\right]\frac{\left(\dfrac{d\Delta^i\xi_s}{d\alpha}\right)_{B.L.}}{\dfrac{d\Delta^i\xi_s}{d\alpha}}\right.$$

$$\left. + \left[\bar{\xi} - \xi_s - \frac{\left(\dfrac{\partial P_s}{\partial\alpha}\right)_{\delta}}{\left(\dfrac{\partial P_{\xi_s}}{\partial\alpha}\right)_{\delta}}\,\frac{U}{(U_e)_s}\right]\frac{\left(\dfrac{\partial\Delta^i\xi_s}{\partial\alpha}\right)_{\delta}}{\dfrac{d\Delta^i\xi_s}{d\alpha}}\right\}\frac{c\dot{\theta}}{U} \tag{3.48}$$

How the unsteady aerodynamic relationships derived above are incorporated in the equations of motion of an elastic vehicle has been described in detail in Refs. 12 and 13. Some of the results of these analyses are shown here to illustrate how the shock-induced separation can affect vehicle dynamics.

Section 4
DISCUSSION

The effect of the shock-boundary layer interaction on the aeroelastic stability at $\alpha < \alpha_{crit}$ is very modest, causing slightly decreased damping (Fig. 4-1). The effect at $\alpha = \alpha_{crit}$, however, is appreciable (Fig. 4-2) and may cause concern especially in regard to aeroelastic stability, where the allowable nose amplitude $\Delta\theta_N$ is small. Figure 4-2 shows separation-induced damping for a Saturn booster in its second bending mode. Using 20° cone data (Refs. 1 and 14), the damping due to accelerated flow effects alone would be as shown. This would represent the total effects at $\alpha_{crit} < 0$, where the boundary-layer buildup effect is negligible.

The loading caused by $\Delta\theta_N$ corresponds roughly to the static loading at an order-of-magnitude higher angle-of-attack ($\alpha_{static} \approx 10\Delta\theta_N$). At $\alpha_{crit} > 0$, the boundary-layer buildup effect becomes dominant and greatly aggravates the undamping effect (Fig. 4-3). For 0.25° nose amplitude, the undamping increases from -0.5 percent at $\alpha_{crit} < 0$ to -1.5 percent at $\alpha_{crit} = 4°$. That there are reasons for concern is obvious. For the structural damping 0.5 percent is a rather typical value, and $\Delta\theta_N = 0.25°$ is probably a representative value for the allowable nose amplitude.

Experimental verification of this undamping effect is hard to come by. Data obtained at the NASA Langley Research Center on an 8-percent elastic model of the Saturn I booster (Ref. 16) indicate the probable occurrence of this phenomenon (Fig. 4-4). The 12.5° Jupiter nose cone by itself would not have experienced any complete separation at reasonable angles-of-attack. However, the presence of the downstream conical frustum with its adverse effects on the forebody pressure gradient is very likely to cause the sudden, complete separation to occur. This would then account for the large drop in damping at $M = 0.9$ for positive angles-of-attack.

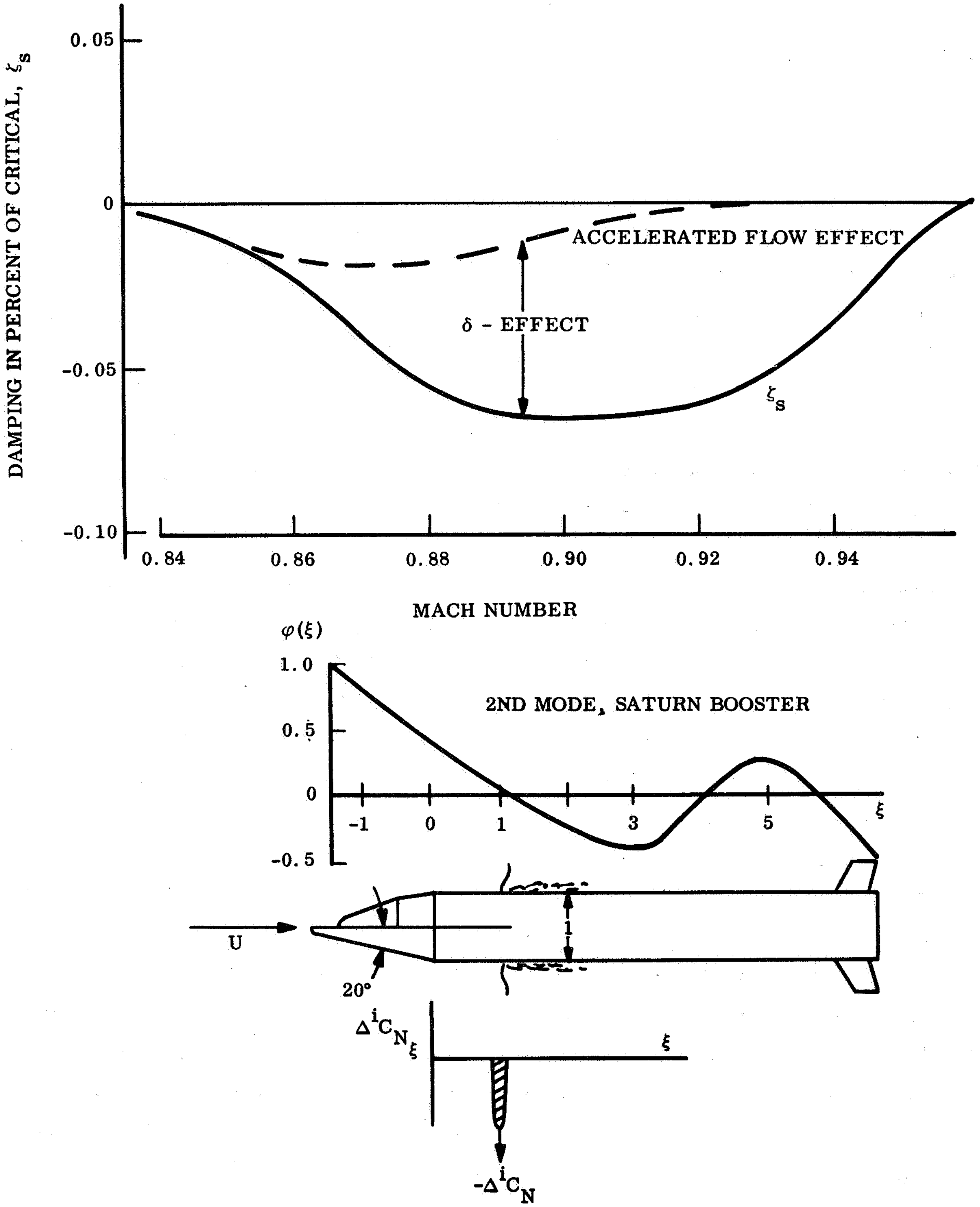

Fig. 4-1 Effect of Separation-Induced Terminal-Shock Movement on the Damping of an Elastic Vehicle Oscillating in Its Second Bending Mode

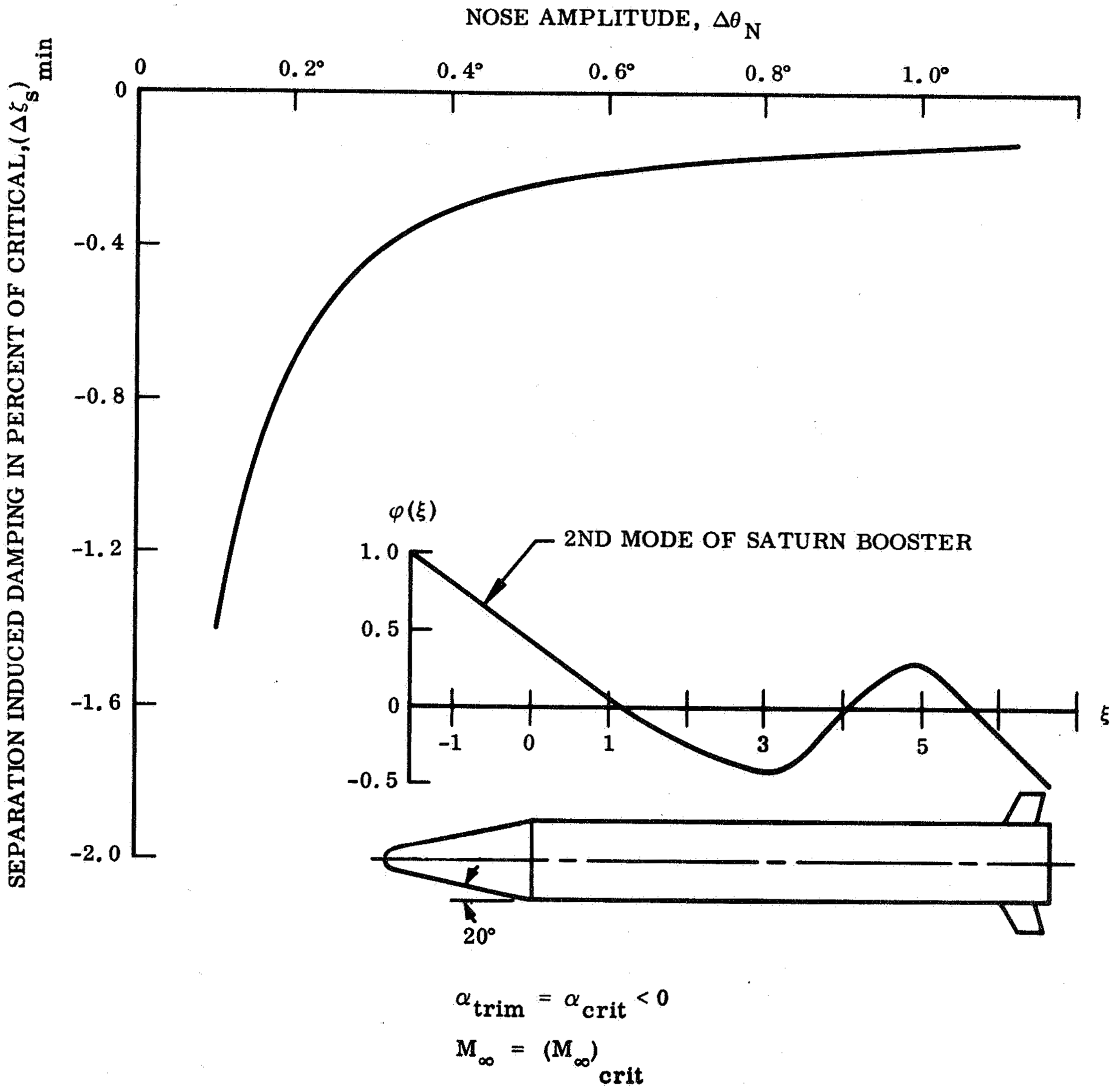

Fig. 4-2 Effect of Complete Leeward-Side Flow Separation in the Damping of an Elastic Vehicle Oscillating in Its Second Bending Mode at Various Nose Amplitudes

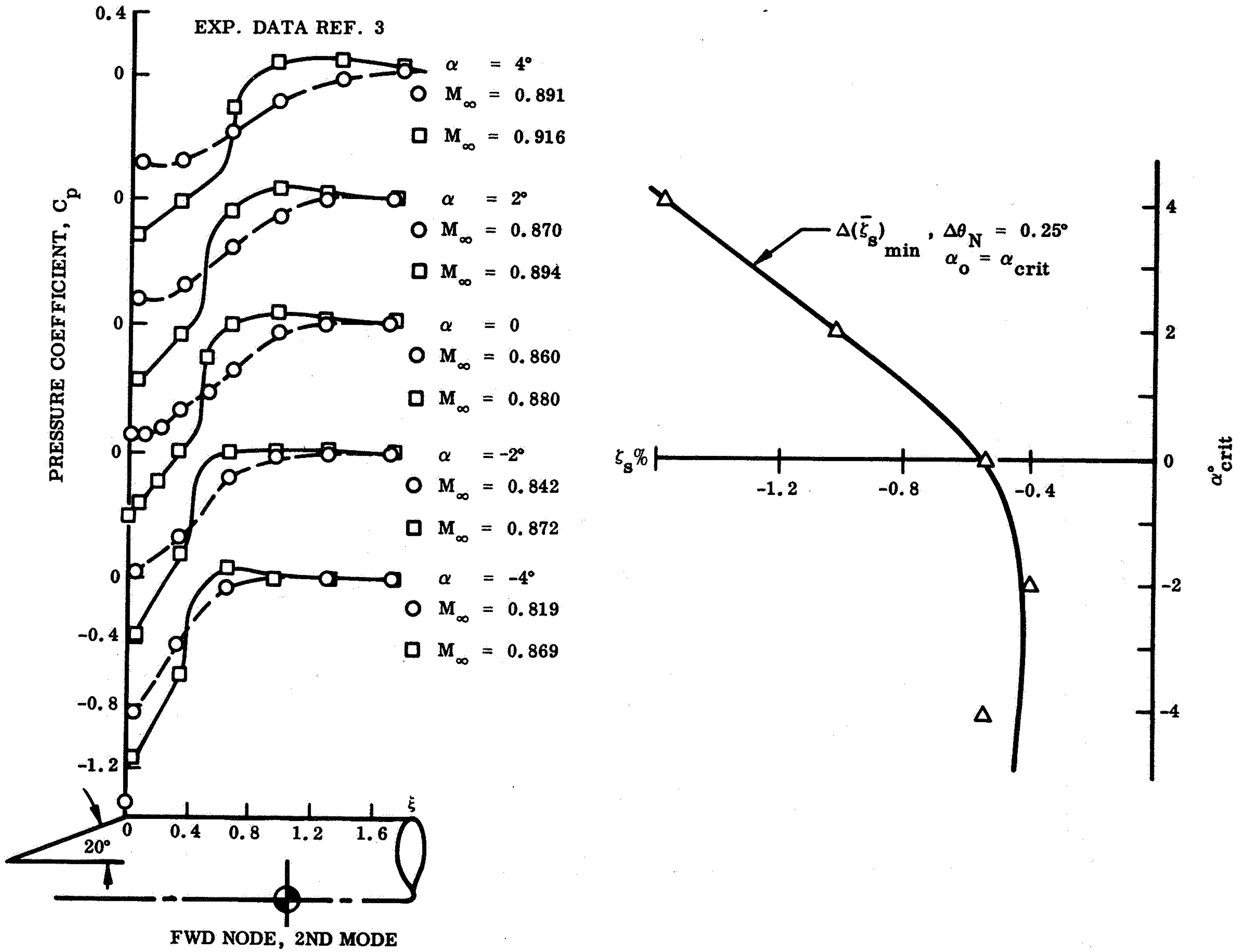

Fig. 4-3 Comparison of Leeward- and Windward-Side Undamping Induced by Complete Flow Separation on an Elastic Vehicle Oscillating in Its Second Bending Mode at 0.25° Nose Amplitude

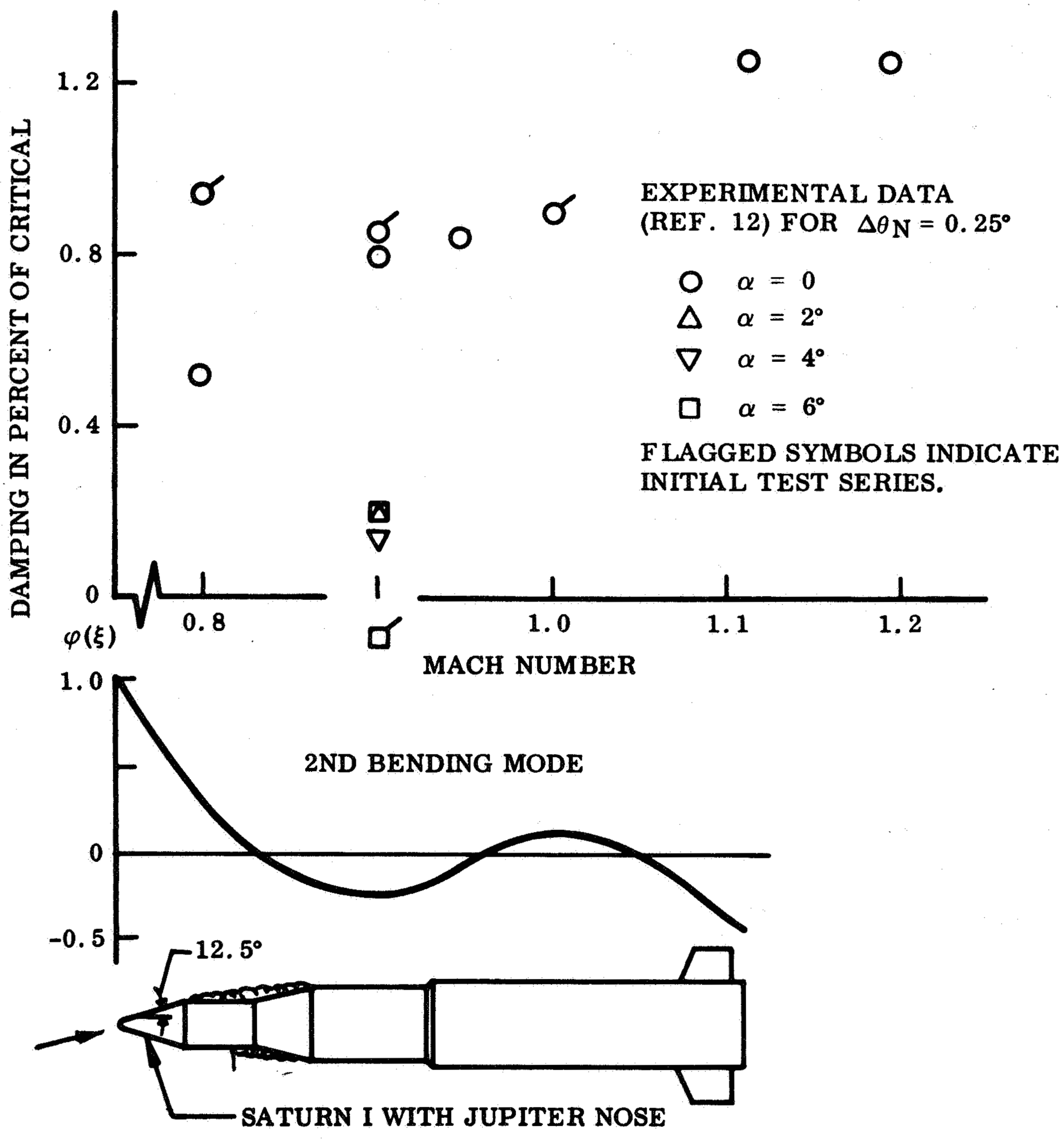

Fig. 4-4 Aerodynamic Damping Measured on an 8-Percent Elastic Model of Saturn I, Block II Vehicle With a Jupiter Nose

A more direct verification of the discussed adverse dynamic effects of the "sudden separation" is provided by dynamic wind-tunnel tests of rigid cylinder-flare bodies (Ref. 17). Figure 4-5 shows the effects of the jumpwise change of flow pattern. Even at the employed amplitudes of above 4°, the effect of catching the jump are drastic. The separation-induced load change on a cylinder-flare body with a hemispherical nose (Fig. 4-6) shows great similarity to the slender payload phenomenon (Fig. 2-1). The associated undamping effect (Fig. 4-7) was largely due to the induced flare load with its additional time lag effect (Ref. 17) – the time delay before the separation affects the flare after it has taken place locally at the nose. The accelerated flow effect was neglected on the cylinder-flare bodies (Ref. 17). However, the accelerated flow effects may well have been nonnegligible and could provide a more plausible explanation than the shown 1° static α-hysteresis (Fig. 4-7).

It is certain that the "sudden separation" has a greatly undamping effect, and that the effect could be catastrophic on an elastic vehicle (i.e., if the separation is caught). If one considers this effect catchable only at discrete α-M_∞-combinations, represented by the boundaries shown in Fig. 3-17, then the probability of an aeroelastic catastrophe is small indeed. However, in the regions of alternating flow, shown in Fig. 3-17, the random separation occurrence for a fixed model (Refs. 14 and 18) does not preclude the possibility that an oscillating model would drive the separation. It is not unlikely that the alternating flow described by Chevalier and Robertson is nothing but a body-flow response to a random disturbance at $\alpha_o = \alpha_{crit}$, e.g., a tunnel flow disturbance. In that case, the regions shown in Fig. 3-17 would represent the aeroelastic danger zones, making the problem a great deal more serious.

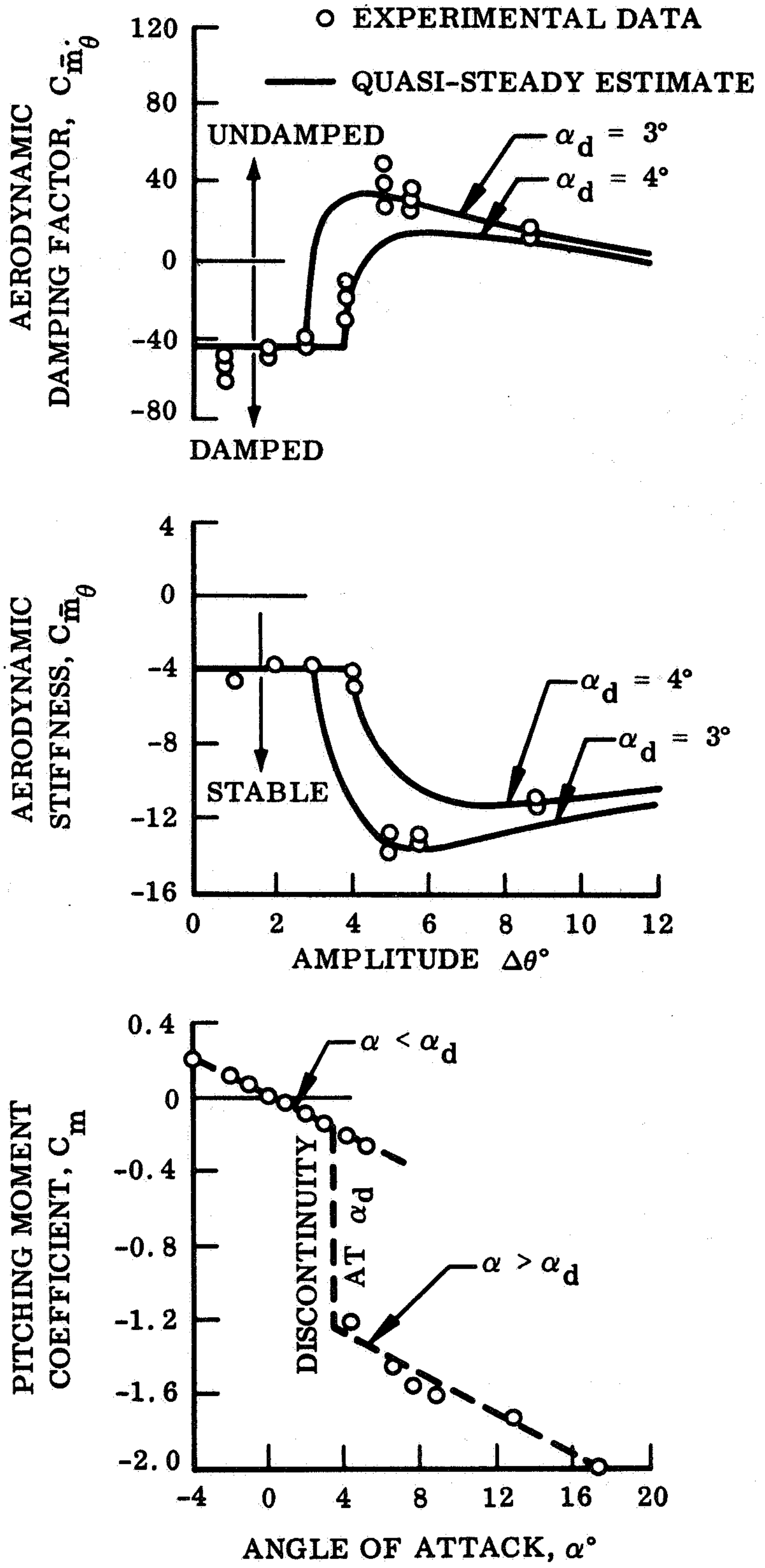

Fig. 4-5 Dynamic Effects of Separation-Induced Pitching-Moment Discontinuity on a Blunt-Nose, Cylinder-Flare Body at Transonic Speed

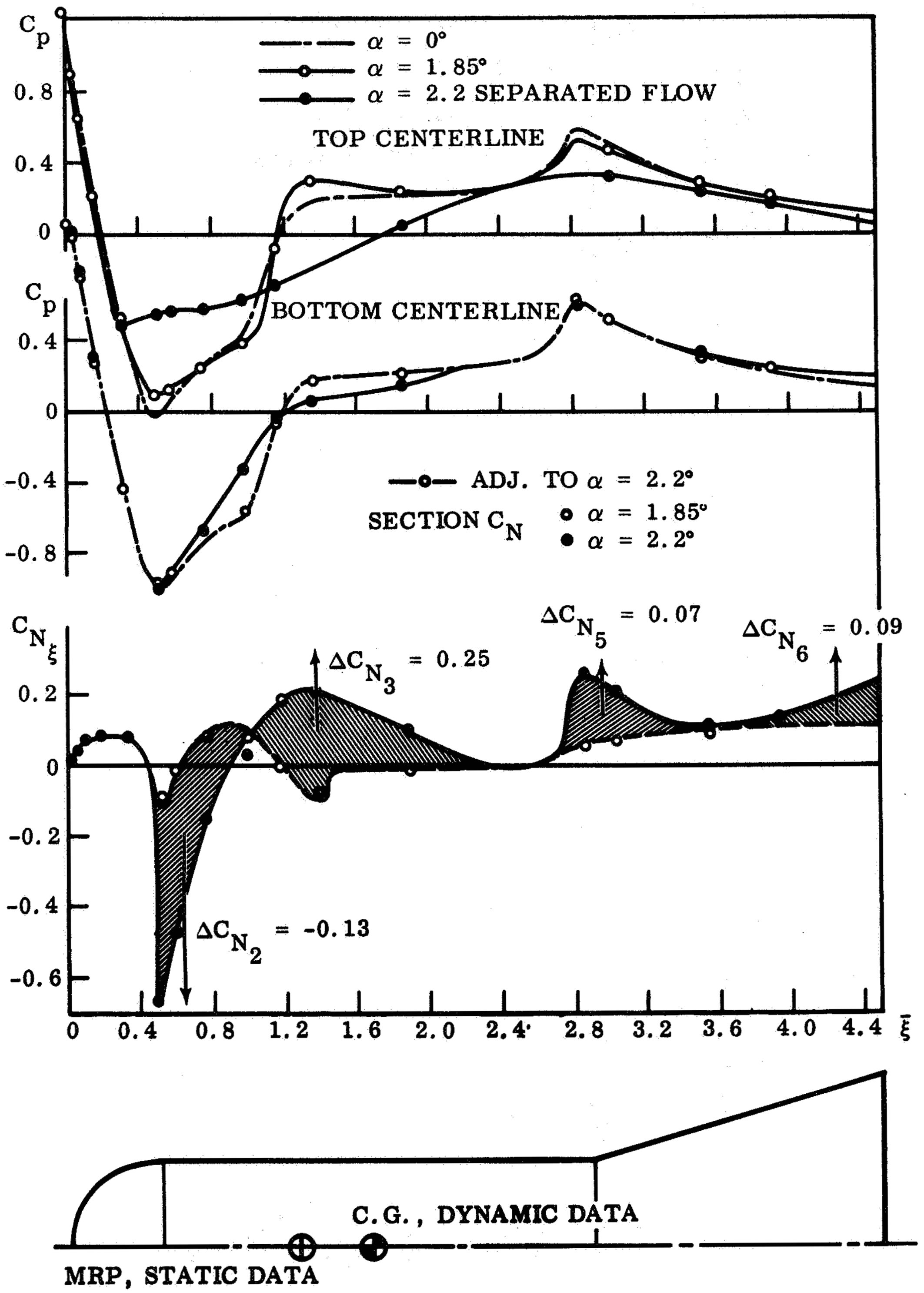

Fig. 4-6 Effect of Complete Leeward-Side Separation on Pressure and Load Distribution Over a Hemispherical-Nose, Cylinder-Flare Body at M_∞ = 0.95

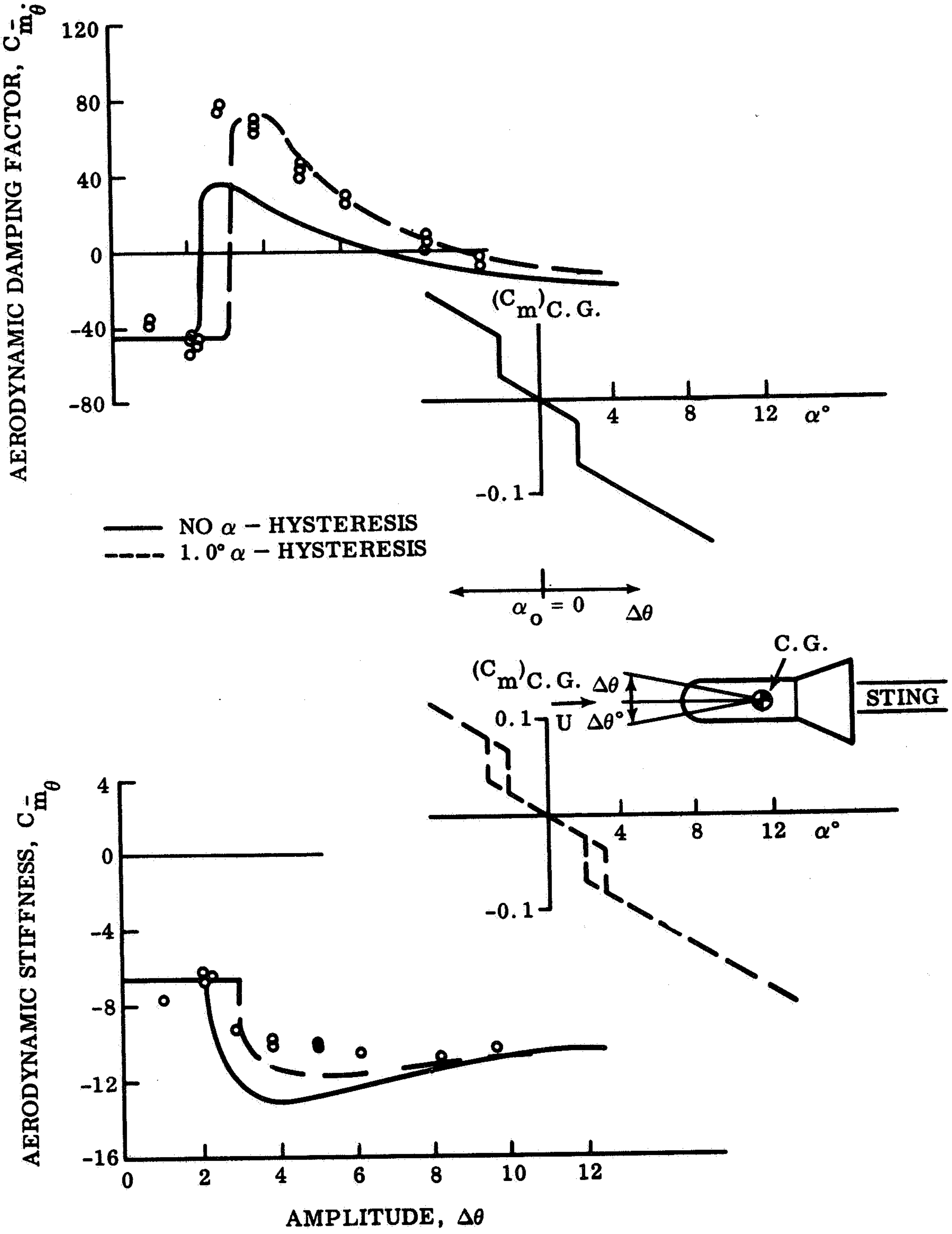

Fig. 4-7 Dynamic Effect of Separation-Induced Pitching-Moment Discontinuity on a Hemispherical-Nose, Cylinder-Flare Body at $M_\infty = 0.95$

Section 5
CONCLUSIONS

Slender cone-cylinder bodies are at high subsonic speeds subject to boundary-layer separation caused by the normal shock terminating the local supersonic flow region aft of the cone-cylinder shoulder. This separation can be a problem for elastic launch vehicles.

A conical payload, even with a half-angle of 15° or less, can have two kinds of aeroelastically destabilizing effects at high subsonic speeds. One is a commonly occurring linear, moderately undamping effect caused by the continuous interaction between the terminal shock and the separating boundary layer on the booster just aft of the cone-cylinder juncture. The other is a rarely occurring nonlinear, immensely undamping effect caused by the discontinuous load change due to a sudden jump forward of the flow separation to the cone-cylinder shoulder. Analytical methods are developed that relate steady and unsteady aerodynamic characteristics for the two types of separation.

Section 6
REFERENCES

1. Arnold Engineering Development Center, Characteristics of Steady-State Pressures on the Cylindrical Portion of Cone-Cylinder Bodies at Transonic Speeds, by J. E. Robertson and H. L. Chevalier, AEDC TDR 63-104, Aug 1963
2. D. M. Jecmen, J. P. Reding, and L. E. Ericsson, "An Application of Automatic Carpet Plotting to Wind Tunnel Data Reduction," J. Spacecraft and Rockets, Vol. 4, 1967, pp. 408–410
3. Lockheed Missiles & Space Company, Automatic Carpet Plotting, by D. M. Jecmen, LMSC-805634, Sunnyvale, Calif., Jan 1967
4. L. E. Ericsson and J. P. Reding, "Analysis of Flow Separation Effects on the Dynamics of a Large Space Booster," J. of Spacecraft and Rockets, Vol. 2, Jul–Aug 1965, pp. 481–490
5. Lockheed Missiles & Space Company, Dynamics of Separated Flow Over Blunt Bodies, by L. E. Ericsson and J. P. Reding, LMSC 2-80-65-1, Sunnyvale, Calif., Dec 1965
6. National Advisory Committee for Aeronautics, Equations, Tables, and Charts for Compressible Flow, by A. R. Staff, NACA Rpt. 1135, Moffett Field, Calif., 1953
7. -----, A Second-Order Shock-Expansion Method Applicable to Bodies of Revolution Near Zero Lift, by Clarence A. Syvertson and David H. Dennis, NACA Report 1328, 1957
8. National Aeronautics and Space Administration, Investigation at Transonic Mach Numbers of the Effects of Configuration Geometry on Surface Pressure Distributions for a Simulated Launch Vehicle, by Thomas C. Kelly, NASA TM X-845 Aug 1963 (C)

9. Arnold Engineering Development Center, Steady and Unsteady Pressures on Cone-Cylinder Missile Configurations at Transonic Speeds, by J. E. Robertson, AEDC TR-65-269, Feb 1966
10. H. Schlichting, Boundary Layer Theory, New York, McGraw Hill, 1955
11. Ballistic Research Laboratory, The Transition From a Turbulent to a Laminar Boundary Layer, by Joseph Sternberg, BRL Report No. 906, May 1964
12. Lockheed Missiles & Space Company, The Aeroelastic Characteristics of the Saturn IB Launch Vehicle With Biconic Payload Shroud, by L. E. Ericsson, N. J. French, and R. A. Guenther, LMSC M-37-67-1, Sunnyvale, Calif., Jul 1967
13. L. E. Ericsson, "Aeroelastic Instability Caused by Slender Payloads," J. Spacecraft and Rockets, Vol. 4, 1967, pp. 65–73
14. Arnold Engineering Development Center, Pressure Fluctuations Resulting from Alternating Flow Separation and Attachment at Transonic Speeds, by H. L. Chevalier and J. E. Robertson, AEDC TDR 63-204, Nov 1963
15. W. V. Speaker and C. M. Ailman, "Static and Fluctuating Pressures in Regions of Separated Flow," AIAA Preprint 66-456 (paper presented at AIAA 4th Aerospace Sciences Meeting, Los Angeles, Calif., 7–29 Jun 1966)
16. National Aeronautics and Space Administration, Aerodynamic Damping and Buffet Response of an Aeroelastic Model of the Saturn I Block II Launch Vehicle, by Perry W. Hanson and Robert V. Dogget, Jr., NASA TND-2713, Mar 1965
17. Lockheed Missiles & Space Company, Separated Flow Effects on the Dynamic Stability of Blunt-Nosed Cylinder-Flare Bodies, by L. E. Ericsson, LMSC-667991, Sunnyvale, Calif., Dec 1965
18. Jack E. Robertson, "Unsteady Pressure Phenomena for Basic Missile Shapes at Transonic Speeds," AIAA Preprint No. 64-3 (paper presented at AIAA 1st Aerospace Sciences Meeting, New York, 20–22 Jan 1964)

19. National Aeronautics and Space Administration, Linear Aerodynamic Loads on Cone-Cylinders at Mach Numbers from 0.7 to 2.0, by R. L. Hammer and A. D. Leff, NASA CR-413, Lockheed Missiles & Space Company, Huntsville, Ala., Mar 1966

Appendix A
NOMENCLATURE

Variables and Constants

a	speed of sound, m/sec
c	reference length or cylinder caliber, m
H	total pressure, kg/m^2
L_1	boundary-layer shape factor
M	Mach number (U/a)
M	pitching moment, kgm [coefficient $C_m = M/(\rho U^2/2)\,Sc$]
N	normal force, kg [coefficient $C_N = N/(\rho U^2/2)\,S$]
p	static pressure, kg/m^2 [coefficient $C_p = (p - p_\infty)/(\rho U^2/2)$]
P	static pressure ratio, $P = \dfrac{p - p_\infty}{H_\infty}$
S	reference area, $\pi c^2/4$
t	time, sec
U	vehicle velocity, m/sec
$\bar{U}$	convection velocity, m/sec [see Eq. (3.38)]
w	crossflow, m/sec
x	horizontal coordinate, m
x_1	axial coordinate, m
α	angle-of-attack, radian or deg
α_o	trim angle-of-attack, radian or deg
$\tilde{\alpha}$	local crossflow angle, radian or deg

γ	specific heat ratio ($\gamma = 1.4$ for air)
δ	boundary-layer thickness, m
δ^*	boundary-layer displacement thickness, m
Δ	incremental difference
ϵ	small fraction [see Eq. (B.12)]
ζ	structural damping, fraction of critical
ζ_s, ζ_a	aerodynamic damping, fraction of critical
θ	body attitude, radian or deg
θ_c	cone half-angle, radian or deg
ν	Prandtl-Meyer expansion angle, radian
ξ	dimensionless coordinate x_1/c
ρ	density of air, kg sec^2/m^4
ψ	azimuth angle, radian

Subscripts

a	attached flow
AC	aerodynamic center
B.L.	due to boundary-layer buildup
c and crit	critical
cyl	cylinder
C	total cylinder load
d	discontinuity
e	local external flow
N	nose

o	at $\xi = o$
o	at α close to zero
p	due to pressure gradient buildup
s	separated flow or shock wave in separated flow
sh	shock wave in attached flow
∞	undisturbed flow

Superscripts

i	induced, e.g., $\Delta^{i}C_N$ = separation-induced normal force coefficient

Differential Symbols

$$P_{\xi} = \frac{\partial P}{\partial \xi}$$

$$\dot{\theta}(t) = \frac{\partial \theta}{\partial t}$$

$$C_{N_{\alpha}} = \frac{dC_N}{d\alpha}$$

$$\left(\frac{\partial C_N}{\partial \alpha}\right)_{\delta} = \frac{\partial C_N}{\partial \alpha} \text{ at } \delta = \text{constant}$$

$$\left(\frac{d\Delta^{i}\xi_s}{d\alpha}\right)_{\text{B. L.}} = \frac{d\Delta^{i}\xi_s}{d\alpha} \text{ at constant inviscid pressure gradient}$$

$$C_{m_{\dot{\theta}}} = \frac{\partial C_m}{\partial \frac{c\dot{\theta}}{U}}$$

Appendix B
SHOCK-INDUCED CYLINDER LOADS

The normal force loading on the cylinder between stations ξ_1 and ξ_2 is in coefficient form (see sketch in Fig. B-1).

$$C_{N_{cyl}} = -\frac{4}{\pi} \int_{\xi_1}^{\xi_2} 2 \int_{-\pi/2}^{\pi/2} C_p(\xi, \psi)\, 0.5 \sin\psi\, d\psi\, d\xi \qquad \text{(B.1)}$$

with

$$C_p = P/\frac{\gamma}{2} M_\infty^2 (p_\infty/H_\infty) \qquad \text{(B.2)}$$

The corresponding normal force derivative is

$$\left(C_{N_\alpha}\right)_{cyl} = -\frac{4/\pi}{\frac{\gamma}{2} M_\infty^2 (p_\infty/H_\infty)} \int_{\xi_1}^{\xi_2} \int_{-\pi/2}^{\pi/2} P_\alpha(\xi, \psi) \sin\psi\, d\psi\, d\xi \qquad \text{(B.3)}$$

According to Eqs. (3.6) and (3.8),

$$P_\alpha(\xi, \psi) = \frac{\partial P_o}{\partial \alpha} e^{-\xi/\xi_o} \qquad \text{(B.4)}$$

p_o/H_∞ is given by Eq. (3.8a) where θ_c now includes the α-effect, i.e.,

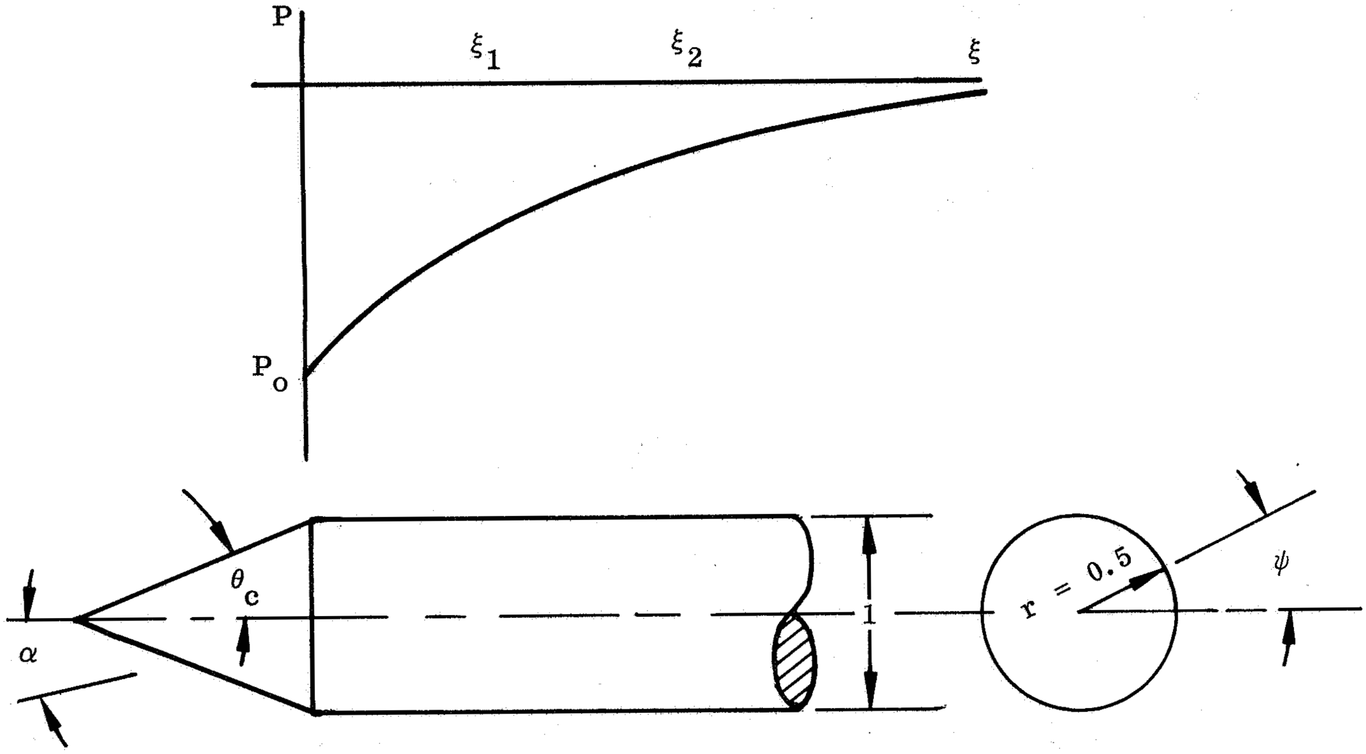

Fig. B-1 Shock-Free Pressure Distribution

$$\left(\theta_c\right)_{\text{effective}} = \theta_c + \alpha \sin\psi$$

Thus P_α becomes

$$P_\alpha(\xi, \psi) = -2.7\, P_o(\theta_c)\, e^{-\xi/\xi_o} \sin\psi \tag{B.5}$$

and Eq. (B.3) gives

$$C_{N_{\alpha_{cyl}}} = -\frac{5.4\, P_o(\theta_c)\, \xi_o}{\frac{\gamma}{2} M_\infty^2 (p_\infty/H_\infty)} \left[e^{-\xi_2/\xi_o} - e^{-\xi_1/\xi_o}\right] \tag{B.6}$$

For a long cylinder, the total cylinder load is $(\xi_2 \rightarrow \infty,\ \xi_1 = 0)$

$$C_{N_{\alpha_C}} = -\frac{5.4\, P_o(\theta_c)\, \xi_o}{\frac{\gamma}{2} M_\infty^2 (p_\infty/H_\infty)} \tag{B.7}$$

With a terminal shock standing at ξ_{sh} the attached flow-pressure distribution is as sketched in Fig. B-2. The pressure jump is, by Eqs. (3.6) and (B.2),

$$\Delta C_{p_{sh}} = -\frac{P_o(\theta_c)}{\frac{\gamma}{2} M_\infty^2 (p_\infty/H_\infty)}\, e^{-\xi_{sh}/\xi_o} \tag{B.8}$$

Assuming a constant pressure jump gives the following shock-induced load derivative when the shock is moved because of angle-of-attack effects:

$$\Delta C_{N_{\alpha_{sh}}} = \frac{P_o(\theta_c)}{\frac{\gamma}{2} M_\infty^2 (p_\infty/H_\infty)}\, e^{-\xi_{sh}/\xi_o}\, \frac{d\xi_{sh}}{d\alpha} \tag{B.9}$$

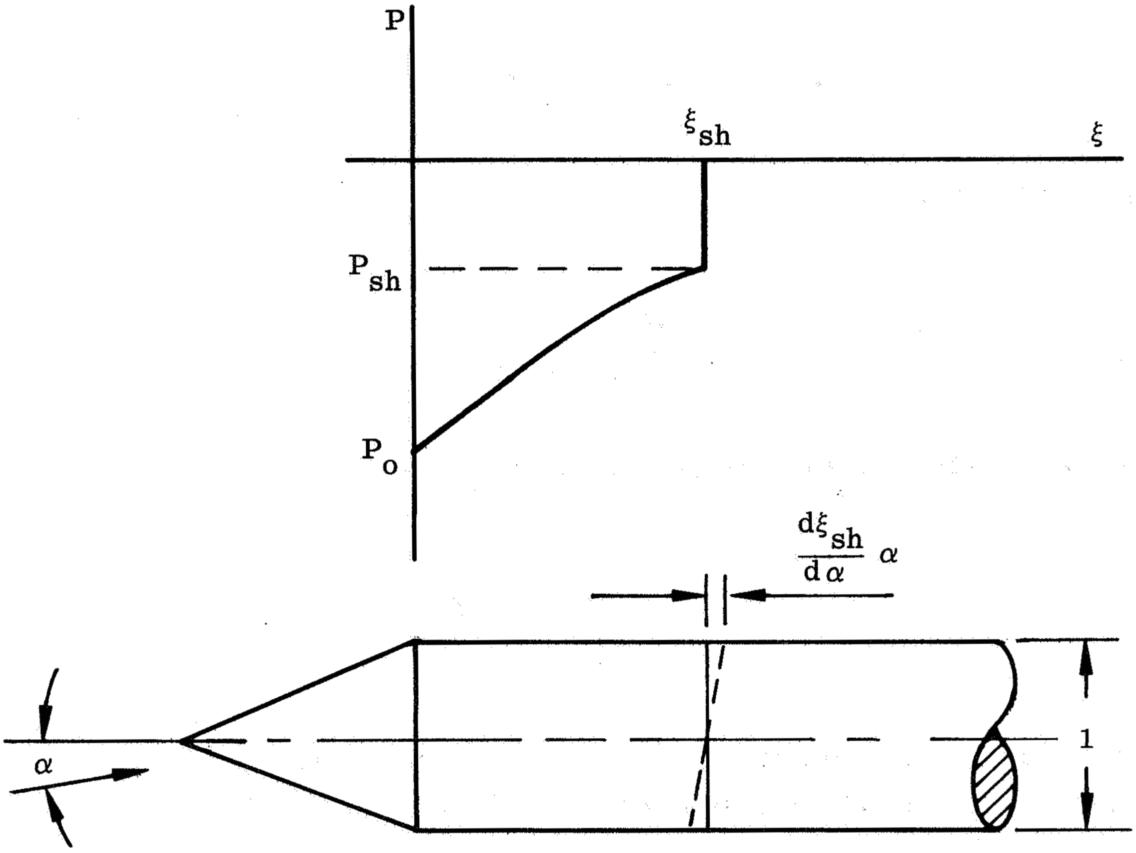

Fig. B-2 Attached Flow-Pressure Distribution With Terminal Shock

The total load on the cylinder in attached flow is then

$$\left(C_{N_{\alpha_C}}\right)_{sh} = C_{N_{\alpha_C}}(\xi_{sh}) + \Delta C_{N_{\alpha_{sh}}}$$

where $\Delta C_{N_{\alpha_{sh}}}$ is given by Eq. (B.9) and $C_{N_{\alpha_C}}(\xi_{sh})$ is given by Eq. (B.6) with $\xi_2 = \xi_{sh}$, $\xi_1 = 0$, i.e.,

$$\left(C_{N_{\alpha_C}}\right)_{sh} = -\frac{P_o(\theta_c)}{\frac{\gamma}{2} M_\infty^2 (p_\infty/H_\infty)} \left[5.4\,\xi_o - \left(5.4\,\xi_o - \frac{d\xi_{sh}}{d\alpha}\right) e^{-\xi_{sh}/\xi_o}\right] \qquad \text{(B.10)}$$

Correspondingly, the total cylinder load in separated flow is

$$\left(C_{N_{\alpha_C}}\right)_{s} = C_{N_{\alpha_C}}(\xi_s) + \Delta C_{N_{\alpha_s}}$$

and is given by Eq. (B.10) if ξ_s is substituted for ξ_{sh}. The separation-induced force is

$$\Delta^i C_{N_\alpha} = \left(C_{N_{\alpha_C}}\right)_s - \left(C_{N_{\alpha_C}}\right)_{sh}$$

or

$$\Delta^i C_{N_\alpha} = - \frac{P_o(\theta_c)\, e^{-\xi_s/\xi_o}}{\frac{\gamma}{2} M_\infty^2 \,(p_\infty/H_\infty)} \left[\frac{d\Delta^i \xi_s}{d\alpha} + \left(\frac{d\xi_{sh}}{d\alpha} - 5.4\, \xi_o \right) \left(1 - e^{\Delta^i \xi_s/\xi_o} \right) \right] \qquad \text{(B.11)}$$

where

$$\Delta^i \xi_s = \xi_s - \xi_{sh}$$

and

$$- \frac{P_o(\theta_c)\, e^{-\xi_s/\xi_o}}{\frac{\gamma}{2} M_\infty^2 \,(p_\infty/H_\infty)} = \Delta C_{p_s}$$

is the pressure jump through the normal shock in coefficient form. Thus, $\Delta^i C_{N_\alpha}$ can be expressed as

$$\Delta^i C_{N_\alpha} = \Delta C_{p_s} \frac{d\Delta^i \xi_s}{d\alpha} + \epsilon\, \Delta C_{N_\alpha} \qquad \text{(B.12)}$$

where

$$\Delta C_{N_\alpha} = - \frac{P_o(\theta_c)}{\frac{\gamma}{2} M_\infty^2 \,(p_\infty/H_\infty)} \left(5.4\, \xi_o - \frac{d\xi_{sh}}{d\alpha} \right)$$

is the difference between the attached flow cylinder loading without and with normal shocks and

$$\epsilon = 1 - e^{-\Delta^i \xi_s / \xi_o} = \frac{\Delta^i \xi_s}{\xi_o} - \frac{1}{2}\left(\frac{\Delta^i \xi_s}{\xi_o}\right)^2 ---$$

is a fraction less than $\Delta^i \xi_s / \xi_o$. That is, neglecting the term $\epsilon \Delta C_{N_\alpha}$ in Eq. (B.12) amounts to neglecting a few percent of the attached flow type loading, i.e., loads that in the unsteady case have no associated lag. Hence, only a few-percent error in the unsteady loading results when $\epsilon \Delta C_{N_\alpha}$ is neglected.